Two-photon coupling via Josephson element. II. Interaction dressing, cross-Kerr coupling, and limits of the low-energy bosonic model

E. V. Stolyarov [1,*] V. L. Andriichuk [2] and A. M. Sokolov [2,†]

[1] *Quantum Optics and Quantum Information Group, Bogolyubov Institute for Theoretical Physics, National Academy of Sciences of Ukraine, vul. Metrolohichna 14-b, Kyiv 03143, Ukraine*

[2] *Institute of Physics of the National Academy of Sciences, pr. Nauky 46, Kyiv 03028, Ukraine*

(Received 6 October 2025; revised 15 April 2026; accepted 6 October 2026; published 3 November 2026)

We study the interactions mediated by a symmetric superconducting quantum interference device (SQUID), their renormalizations, and the applicability of the anharmonic oscillator (bosonic) model for a coupled phase qubit. The latter dwells in its metastable well holding a number of anharmonic energy states. The coupling SQUID can switch between the single- and two-photon interactions *in situ*. We find that, in the bosonic two-photon regime, the cross-Kerr coupling never vanishes as it dresses due to asymmetry in the qubit potential and nonlinearity of the coupler. Our quantitative results also depend on the bosonic approximation. We approach determining its limits by finding the minimum number of coherent energy states required for a dressing. For that, we lay out diagrams of the dressing virtual processes that climb the qubit ladder as high as possible. Near the two-photon resonance with a coupled resonator, we systematically calculate other relevant renormalizations due to nonresonant interactions. We provide verifiable predictions for the coupling rates. Modified systems can be applied for two-photon detection and for quantum-nondemolition readout of a qubit with an asymmetrical potential.

DOI: 10.1103/znff-859f

I. INTRODUCTION

In a curious prediction of quantum theory, a real transition may occur in two steps with an intermediate state never occupied considerably; the two legs of such a process are called *virtual* transitions. In fact, one can even describe the simplest excitation exchange due to linear interaction, as in the Jaynes-Cummings model [1], in terms of two virtual processes: one destroying a quantum in the first system, and the other creating it in another system. In the respective approximation, the combined system is never found in the intermediate state. In a less trivial example, two nonresonant exchange interactions with an auxiliary system mediate a real excitation exchange between two other systems [2]; a modification [3,4] of such a coupler powers a commercial quantum computer [5].

Virtual transitions can chain into more complex processes as well. Combined with intrinsic nonlinearity and transitions to the higher excited levels, linear interactions between transmon qubits [6] give rise to ZZ interaction [7]. Essentially, ZZ coupling is due to parametric processes [8] in which the system state does not change, but the system energy acquires dependency on the state of its parts. In the context of cavity [9,10] and circuit quantum electrodynamics [11–13], an analogous coupling is known as dispersive. It arises due to virtual transition of a resonator photon into the qubit and back [12].

Two-photon coupling [14–20] allows an electromagnetic degree of freedom to give up two photons in order to produce a single excitation in another system. It can emerge—perturbatively—due to intermediate virtual processes as predicted [16,17,21–23] and measured [21] for different systems. This type of nonlinear coupling can already find some applications. Two-photon interaction facilitates single-mode squeezing [24]. It may be used for novel quantum information processing protocols [19] and achieving photon-number resolution in microwave photodetection [22,23,25]. With a deep strong two-photon coupling, interaction-induced spectral collapse may be observed [26].

To achieve high two-photon coupling rates, one can either "simulate" the coupling using special driving schemes [24], or seek a strong nonlinear interaction. In the preceding contribution [20], we argued that a symmetrical dc superconducting quantum interference device (SQUID) can mediate nonperturbative two-photon coupling of reasonable strength that arises directly from the Josephson nonlinearity. Independently, Ayyash *et al.* conveyed the same point in Ref. [19] for an asymmetrical SQUID. The latter is better suited for coupling circuits with zero static displacement of the superconducting condensate phase over them, such as resonator and transmon [6] qubits. However, in both works [19,20], only the bare two-photon coupling was calculated; i.e., the two-photon transitions due to possible virtual processes were not accounted for.

Moreover, neither of the works considered the cross-Kerr coupling. It arises with a parametric process, similarly to the

*Contact author: eugene.stolyarov@bitp.kyiv.ua

†Contact author: andriy145@gmail.com

Published by the American Physical Society under the terms of the Creative Commons Attribution 4.0 International license. Further distribution of this work must maintain attribution to the author(s) and the published article's title, journal citation, and DOI.

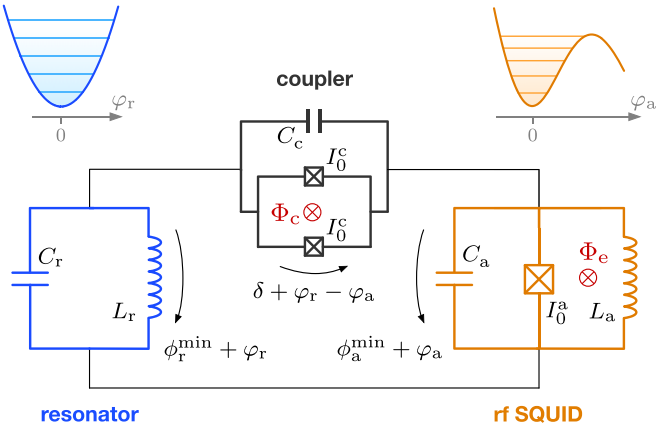


FIG. 1. A resonator and an rf SQUID in the regime where the phase qubit interacts through the SQUID coupler. The system evolves around the equilibrium phase differences ϕ_r^{min} and ϕ_a^{min}. The respective varying departures are φ_r and φ_a. Conjugate to them, dynamic variables n_r and n_a are the Cooper pair number at the full capacitances. $\delta = \phi_r^{min} - \phi_a^{min}$ is the equilibrium phase difference over the coupler. Φ_c and Φ_e are the coupler and rf SQUID bias fluxes. Cartoons show potentials and energy levels of the resonator (left) and the phase qubit (right).

ZZ or dispersive coupling mentioned above. Typically, the term is used for two systems each having many energy states. With the cross-Kerr coupling, the combined energy acquires a contribution proportional to each of the system populations. This can be detrimental for implementing two-qubit gates [4,27–29], applications of optomechanical systems [30], and in traveling-wave parametric amplifiers [31]. In the absorbing detectors of microwave photons [32–43], cross-Kerr coupling introduces a photon-number–dependent detuning that may complicate the absorption. On the other hand, this very type of coupling is required for the quantum-nondemolition detection [44–51], dispersive qubit readout [11], and other applications for quantum computing with superconducting circuits [52,53]. The cross-Kerr coupling can be used to simulate optomechanical coupling using an additional driven mode [54].

It seems that the cross-Kerr interaction can be switched off in a Josephson coupler, as in Refs. [20,25,55,56]. The coupler mediates interactions between the "coordinates" φ_r and φ_a via its potential energy, proportional to $\cos(\varphi_r - \varphi_a + \delta)$, where δ is some equilibrium phase. To achieve higher values of the bare two-photon interaction, one can set $\delta = \pi/2$ to maximize the $\varphi_r^2\varphi_a$ expansion term in the energy [20,55]. At the same time, one may expect that the cross-Kerr coupling is absent. Indeed, the bare cross-Kerr coupling only arises from the even-order expansion terms, absent at $\delta = \pi/2$.

In this work, we continue to study a resonator and a phase qubit coupled via the SQUID coupler (see Fig. 1). Using the bosonic approximation, we devise a systematic theory to answer three questions: (i) Having a plethora of different interactions and nonlinearities in that system, do they produce virtual transitions that yield a considerable correction to the two-photon coupling? (ii) Analogously, are there sizable corrections in the cross-Kerr coupling? Can one mitigate this coupling, and if not, how big is it? (iii) For the virtual processes in the corrections, how many energy levels are required in the qubit metastable well?

The paper is organized as follows: We review the physics and the main parameters of the circuit in Sec. II and discuss important bare interactions in Sec. III. Then, in Sec. IV, we present the effective two-photon Hamiltonian and outline the approximations we use. In Sec. V, we elucidate how the two-photon and cross-Kerr interactions are renormalized by other couplings. We provide some involved virtual processes in the form of diagrams. In Sec. VI, we estimate the coupling rates for a reasonable set of circuit parameters. Section VII discusses our results and their applicability, including the bosonic approximation. We assess some applications and discuss generalizations of the theory in Sec. VIII and conclude in Sec. IX.

We delegate technical details to the Appendixes. In Appendix A, we provide our starting Hamiltonians. Derivation of the effective two-photon Hamiltonian that accounts for all relevant renormalizations is in Appendix B. Appendix C provides an alternative calculation of the main cross-Kerr correction using Wick's theorem. We also provide further detail on laying out the diagrams for the virtual processes involved. In Appendix E, to show that this correction also arises in the classical limit, we use equations of motion to obtain it. Appendix D outlines the recipe for finding the processes that climb the energy ladder as high as possible. Appendix F provides expressions and interpretations for nonessential corrections to the interaction rates.

II. CIRCUIT

It is convenient to describe the circuit dynamics in terms of dimensionless variables. The number of Cooper pairs acts as a generalized momentum while the drop of the superconducting condensate phase acts as a generalized coordinate.

Consider the circuit in Fig. 1. For the isolated resonator, n_r is the Cooper pair number on its capacitance C_r. Analogously, n_a is the number of pairs on the rf SQUID at full capacitance. Near equilibrium, only the departures from the static values of the condensate phases matter. φ_a represents such a departure of the phase difference across the rf SQUID junction. φ_r is the phase departure across the resonator contacts.

We are interested in coupling between the resonator and the rf SQUID acting as an artificial atom. The SQUID coupler mediates linear and nonlinear interactions. Its Josephson energy

$$E_J^c = 2E_{1J}^c \cos\frac{\pi\Phi_c}{\Phi_0} \tag{1}$$

can be tuned by the coupler bias Φ_c. On the other hand, it is set by the Josephson energy of each of the coupler junctions, $E_{1J}^c = I_0^c\Phi_0/2\pi$, where I_0^c is the critical current of the junction and $\Phi_0 = h/2e$ is the flux quantum. The Josephson coupling energy reads $-E_J^c\cos(\varphi_r - \varphi_a + \delta)$, where the static phase difference over the coupler

$$\delta = \phi_r^{min} - \phi_a^{min} - \frac{\pi\Phi_c}{\Phi_0} \tag{2}$$

depends on its bias flux Φ_c. We denote the resonator and atom equilibrium phases by ϕ_r^{min} and ϕ_a^{min}. The equilibrium is determined by the conservation of static currents as expressed in

TABLE I. Important bare interactions in the fourth-order approximation of the Josephson energy. In the diagrams, wavy lines stand for creation or annihilation of a resonator photon while straight lines denote the atom processes. Each line length indicates a change in the system energy. In the two-photon regime, an atom excitation requires twice as much energy as a photonic one. Arrows indicate the start and end of a diagram. Potential asymmetry in the atom brings processes with amplitudes of order $\varphi_{\mathrm{a,zpf}}$ in the atom zero-point fluctuations, as explained in the text. As the diagram acts on a system state from right to left, it recovers the explicitly written term, while acting from left to right yields the H.c. term. Linear coupling: Combined, the capacitive and inductive couplings with rates g_1^c and g_1^i give rise to number-preserving and -nonpreserving exchange processes. Quadratic couplings: A two-photon interaction arises from a quadratic coupling, along with the other ones. Cubic coupling gives rise to the cross-Kerr processes, which are always resonant.

	Energy	Rate	Some processes	
Potential asymmetry	$-\hbar X_{\mathrm{a}}(b^\dagger+b)^3$	$X_{\mathrm{a}}=\frac{\mu}{12}\omega_{\mathrm{a}}^p\varphi_{\mathrm{a,zpf}}$	$X_{\mathrm{a}}bb^\dagger b+\mathrm{H.c.}=X_{\mathrm{a}}$ 	
Linear coupling	Capacitive		Number-preserving	Number-nonpreserving
	$-\hbar g_1^c(a^\dagger-a)(b^\dagger-b)$	$g_1^c=\frac{E_C^{\mathrm{c}}}{\hbar}n_{\mathrm{r,zpf}}n_{\mathrm{a,zpf}}$	$g_-=g_1^c-g_1^i$	$g_+=g_1^c+g_1^i$
	Inductive		$g_-a^\dagger b+\mathrm{H.c.}=g_-$ 	$g_+ab+\mathrm{H.c.}=g_+$
	$-\hbar g_1^i(a^\dagger+a)(b^\dagger+b)$	$g_1^i=\frac{E_J^{\mathrm{c}}}{\hbar}\varphi_{\mathrm{r,zpf}}\varphi_{\mathrm{a,zpf}}\cos\delta$		
Quadratic couplings	$-\hbar g_2(a^\dagger+a)^2(b^\dagger+b)$	$g_2=-\frac{E_J^{\mathrm{c}}}{2\hbar}\varphi_{\mathrm{r,zpf}}^2\varphi_{\mathrm{a,zpf}}\sin\delta$	two-photon: 	Optomechanical:
	$-\hbar G_2(a^\dagger+a)(b^\dagger+b)^2$	$G_2=\frac{E_J^{\mathrm{c}}}{2\hbar}\varphi_{\mathrm{r,zpf}}\varphi_{\mathrm{a,zpf}}^2\sin\delta$	Two–atom-excitation:	Reverse optomechanical:
Cubic coupling	$-\hbar\frac{K_0}{4}(a^\dagger+a)^2(b^\dagger+b)^2$	$K_0=\frac{E_J^{\mathrm{c}}}{\hbar}\varphi_{\mathrm{r,zpf}}^2\varphi_{\mathrm{a,zpf}}^2\cos\delta$	Cross-Kerr: $a^\dagger ab^\dagger b=\frac{1}{2}$ 	

Appendix A 2. Depending on the bias Φ_{c} and the equilibrium position, the Josephson coupling produces inductive linear interaction as well as various nonlinear processes, including the two-photon one [20].

In addition, the coupler charging mediates linear capacitive interaction as in Table I. Its charging energy is

$$E_C^{\mathrm{c}}=4e^2\frac{\tilde{C}_{\mathrm{c}}}{C'_{\mathrm{a}}C_{\mathrm{r}}}, \tag{3}$$

where the coupler capacitance C'_{c} is loaded by the series connection with the resonator and atom capacitances, $\tilde{C}_{\mathrm{c}}=(1/C'_{\mathrm{c}}+1/C_{\mathrm{r}}+1/C'_{\mathrm{a}})^{-1}\approx C'_{\mathrm{c}}$. The latter approximation qualifies as we have $C'_{\mathrm{c}}\ll C_{\mathrm{r}},C'_{\mathrm{a}}$ in Sec. VI, similarly to the preceding work [20]. The full coupling capacitance $C'_{\mathrm{c}}=C_{\mathrm{c}}+2C_{\mathrm{1J}}^{\mathrm{c}}$ consists of the shunt C_{c} and two junction capacitances $C_{\mathrm{1J}}^{\mathrm{c}}$ of the coupler.

We consider charging of the circuit capacitances to accumulate the "kinetic" energy of the circuit. We denote by $E_C^{\mathrm{r}}=e^2/2\tilde{C}_{\mathrm{r}}$ the resonator charging energy, where $\tilde{C}_{\mathrm{r}}=C_{\mathrm{r}}+C'_{\mathrm{a}}C'_{\mathrm{c}}/(C'_{\mathrm{a}}+C'_{\mathrm{c}})$ is the loaded resonator capacitance. That is, C_{r} is loaded by the parallel connection with the atom full capacitance C'_{a}, which is connected in series with the full coupling capacitance C'_{c}. Analogously, the artificial atom charging energy is $E_C^{\mathrm{a}}=e^2/2\tilde{C}_{\mathrm{a}}$, where $\tilde{C}_{\mathrm{a}}=C'_{\mathrm{a}}+C_{\mathrm{r}}C'_{\mathrm{c}}/(C_{\mathrm{r}}+C'_{\mathrm{c}})$ and $C'_{\mathrm{a}}=C_{\mathrm{a}}+2C_{\mathrm{1J}}^{\mathrm{a}}$ is the full atom capacitance. It consists of the shunting capacitance C_{a} and the internal capacitances $C_{\mathrm{1J}}^{\mathrm{a}}$ of each of the atom junctions. We rely on the exact expression for $\tilde{C}_{\mathrm{a}}$ to tune the atom and resonator into the two-photon resonance.

Quadratic potential energy of the circuit arises as it does from linear inductances. The Josephson energy also contributes. The full inductive-like energies read

$$\tilde{E}_L^{\mathrm{r}}=E_L^{\mathrm{r}}+E_{\mathrm{J}}^{\mathrm{c}}\cos\delta, \tag{4a}$$

$$\tilde{E}_L^{\mathrm{a}}=E_L^{\mathrm{a}}+E_{\mathrm{J}}^{\mathrm{a}}\cos\phi_{\mathrm{a}}^{\min}+E_{\mathrm{J}}^{\mathrm{c}}\cos\delta. \tag{4b}$$

Here $E_{\mathrm{J}}^{\mathrm{a}}=I_0^{\mathrm{a}}\Phi_0/2\pi$ is the atom Josephson energy. $E_L^{\mathrm{r}}=\Phi_0^2/4\pi^2L_{\mathrm{r}}$ is the resonator inductive energy, and a similar expression holds for the atom inductive energy. According to Eq. (4a), the resonator inductance L_{r} is loaded by the coupler Josephson inductance, $L_{\mathrm{c}}=\Phi_0^2/(4\pi^2E_{\mathrm{J}}^{\mathrm{c}}\cos\delta)$, as $\tilde{L}_{\mathrm{r}}^{-1}=L_{\mathrm{r}}^{-1}+L_{\mathrm{c}}^{-1}$. Equation (4b) expresses both the load from the coupler and the analogous load from the atom Josephson energy.

The resonator and atom degrees of freedom oscillate around the equilibrium. With the nonlinearities switched off, they oscillate with the plasma frequencies

$$\omega_{\mathrm{r}}^p=\frac{1}{\hbar}\sqrt{8E_C^{\mathrm{r}}\tilde{E}_L^{\mathrm{r}}},\quad \omega_{\mathrm{a}}^p=\frac{1}{\hbar}\sqrt{8E_C^{\mathrm{a}}\tilde{E}_L^{\mathrm{a}}}. \tag{5}$$

Here, the loaded inductive energies $\tilde{E}_L^{\mathrm{r}}$ and $\tilde{E}_L^{\mathrm{a}}$ depend on the equilibrium point as in Eqs. (4).

III. BARE INTERACTIONS

We expand the Josephson energy in the circuit to the fourth order in the resonator and atom phase variables. We provide the expansion in Appendix A after circuit quantization. Here, we focus on the resulting interactions important for this work.

For the expansion of the Josephson energies to be valid, we require that the inductive-type energies dominate over the charging energies:

$$E_L^{\mathrm{r}}\gg E_C^{\mathrm{r}},\quad \tilde{E}_L^{\mathrm{a}}\gg E_C^{\mathrm{a}}. \tag{6}$$

This ensures that the phase particles of both systems are "heavy" and reside close to the equilibrium.

We express the system variables in terms of the bosonic ladder operators: $n_{\mathrm{r}}=in_{\mathrm{r,zpf}}(a^\dagger-a)$ and $\varphi_{\mathrm{r}}=\varphi_{\mathrm{r,zpf}}(a^\dagger+a)$ for the resonator variables, while $n_{\mathrm{a}}=in_{\mathrm{a,zpf}}(b^\dagger-b)$ and $\varphi_{\mathrm{a}}=\varphi_{\mathrm{a,zpf}}(b^\dagger+b)$ for the atom variables. Here, the magni-

tudes of the resonator vacuum fluctuations read

$$n_{\mathrm{r,zpf}} = \left(\tilde{E}_L^{\mathrm{r}}/32E_C^{\mathrm{r}}\right)^{1/4}, \quad \varphi_{\mathrm{r,zpf}} = \left(2E_C^{\mathrm{r}}/\tilde{E}_L^{\mathrm{r}}\right)^{1/4}, \tag{7}$$

and the magnitudes of the atom vacuum fluctuations are

$$n_{\mathrm{a,zpf}} = \left(\tilde{E}_L^{\mathrm{a}}/32E_C^{\mathrm{a}}\right)^{1/4}, \quad \varphi_{\mathrm{a,zpf}} = \left(2E_C^{\mathrm{a}}/\tilde{E}_L^{\mathrm{a}}\right)^{1/4}. \tag{8}$$

In Appendix A 3, we write out the resulting "second-quantized" Hamiltonian in the fourth-order approximation of the Josephson energy.

In Table I, we present the interactions dressing the two-photon, cross-Kerr, and linear coupling. The energy terms in the table yield processes with the given rates or their multiples. We depict some processes with diagrams as explained below.

The cubic nonlinearity $-\hbar X_{\mathrm{a}}(b^\dagger + b)^3$ in the atom potential arises from expansions of both the atom $-E_{\mathrm{J}}^{\mathrm{a}}\cos(\phi_{\mathrm{a}}^{\min} + \varphi_{\mathrm{a}})$ and the coupling Josephson energies. As $E_{\mathrm{J}}^{\mathrm{a}}\varphi_{\mathrm{a,zpf}}^2 = (E_{\mathrm{J}}^{\mathrm{a}}/2\tilde{E}_L^{\mathrm{a}})\hbar\omega_{\mathrm{a}}^p$, the third-order atom term $-(1/3!)E_{\mathrm{J}}^{\mathrm{a}}\varphi_{\mathrm{a,zpf}}^3 \sin\phi_{\mathrm{a}}^{\min}$ turns first order in $\varphi_{\mathrm{a,zpf}}$ if $E_{\mathrm{J}}^{\mathrm{a}} \gtrsim \tilde{E}_L^{\mathrm{a}}$. In that case, we have

$$X_{\mathrm{a}} = \frac{1}{12}\frac{E_{\mathrm{J}}^{\mathrm{a}}}{\tilde{E}_L^{\mathrm{a}}}\omega_{\mathrm{a}}^p\varphi_{\mathrm{a,zpf}}\sin\phi_{\mathrm{a}}^{\min} - \frac{E_{\mathrm{J}}^{\mathrm{c}}}{6\hbar}\varphi_{\mathrm{a,zpf}}^3\sin\delta \tag{9}$$

for the strength of the nonlinearity.

In Table I, this cubic nonlinearity in the atom potential is characterized by

$$\mu = \frac{12X_{\mathrm{a}}}{\varphi_{\mathrm{a,zpf}}\,\omega_{\mathrm{a}}^p} \approx \frac{\sin\phi_{\mathrm{a}}^{\min}}{\cos\phi_{\mathrm{a}}^{\min} + \beta_L^{-1}}, \tag{10}$$

where $\beta_L = E_{\mathrm{J}}^{\mathrm{a}}/E_L^{\mathrm{a}}$ is the screening parameter [57] of the atom loop. When using the expressions in the main part of the paper, to assess only the dominant corrections, one can neglect the coupler contribution as above.

Let us comment on some interactions in Table I. Linear coupling yields number-preserving and -nonpreserving single-photon interactions. In the latter, both the atom and resonator simultaneously excite or deexcite by one energy level.

Consider one of the quadratic couplings from Table I in detail. Expanding, using that $[b, b^\dagger] = 1$, and regrouping, we have

$$\begin{aligned}(a^\dagger + a)^2(b^\dagger + b) = (a^{\dagger 2}b + \mathrm{H.c.}) + (a^2 b + \mathrm{H.c.}) \\ + 2a^\dagger a(b^\dagger + b) + (b^\dagger + b).\end{aligned} \tag{11}$$

The first term on the right-hand side is the energy-preserving (when the frequencies match) part of the two-photon interaction, while the second term is its energy-nonpreserving part. The third term describes a process akin to the optomechanical one [58,59].

Here, in this optomechanical-like interaction, the atom plays the role of an optical cavity. Its frequency is modulated by the generalized coordinate of the microwave resonator that plays the role of a mechanical mode. In the "reverse optomechanical" interaction in Table I, the atom and resonator swap their roles as in Ref. [60].

In Table I, we illustrate some processes with diagrams. For instance, the two-photon diagram depicts the first term on the right-hand side of Eq. (11). The optomechanical diagram depicts, up to a factor of 2, the third term there. Later, we use such diagrams to illustrate the dressing and the minimal number of energy levels it requires.

Note the signs of some energy terms in Table I. We choose them so that the important interaction rates $g_2, K_0 > 0$ when the two-photon coupling strength g_2 attains its highest value (see Fig. 6). That is convenient in what follows, for reading whether the renormalization terms increase or decrease the rate magnitudes. For the same reason, we choose $X_{\mathrm{a}} > 0$ there, as it appears in the rate dressing.

IV. EFFECTIVE MODEL

In this section as well as in the next one, we do not detail the coupler regime. That is, we provide the expressions for the coupling rates for an arbitrary coupler phase δ as given by Eq. (2). We only require that one adjusts the artificial atom and the resonator to the two-photon resonance $\omega_{\mathrm{a}} \approx 2\omega_{\mathrm{r}}$. Here and below in the main text, ω_{a} and ω_{r} stand for the actual, dressed frequencies of the atom and resonator.

A. Two-photon Hamiltonian

In Appendix B, we use Schrieffer-Wolff transformations to derive the system effective Hamiltonian close to the two-photon resonance,

$$\begin{aligned}\frac{\hat{\mathcal{H}}}{\hbar} = \omega_{\mathrm{r}}a^\dagger a + \omega_{\mathrm{a}}b^\dagger b - \frac{\Xi_{\mathrm{a}}}{2}b^{\dagger 2}b^2 \\ - K_{0,X}\,a^\dagger a b^\dagger b - \tilde{g}_2(a^{\dagger 2}b + b^\dagger a^2).\end{aligned} \tag{12}$$

In the rest of this work, the two-photon coupling of rate $\tilde{g}_2$, the cross-Kerr coupling of rate $K_{0,X}$, and the atom anharmonicity Ξ_{a} are most important for us. Due to the two-photon coupling, annihilation of two resonator photons excites the artificial atom, and vice versa. Both rates $\tilde{g}_2$ and $K_{0,X}$ are dressed by the other interactions, as we discuss in the next sections and in Appendix F. In contrast with the standard two-photon Jaynes-Cummings model [61,62], we describe the artificial atom as an oscillator of anharmonicity Ξ_{a} rather than a two-level atom.

According to our preliminary calculations, there are also other, higher-order nonlinearities in Hamiltonian (12) that can be important under reasonable conditions. Namely, they are proportional to $\Xi_{\mathrm{a}}^2 g_-^2/(\omega_{\mathrm{a}} - \omega_{\mathrm{r}})^3$. That is negligible in our case of interest with small anharmonicity $\Xi_{\mathrm{a}} \ll \omega_{\mathrm{r}}, \omega_{\mathrm{a}}$ and the linear coupling g_- suppressed as in Sec. VI E. However, these conditions do not hold in typical circuit quantum-electrodynamic setups with linear coupling, such as, e.g., in Refs. [63,64].

Next, we outline the approximations in the derivation of the effective Hamiltonian. Afterward, in Sec. V, we approximate the two-photon and cross-Kerr interaction rates in the Hamiltonian (12) and approximate the frequencies in Sec. VI C.

B. Approximations and the limits of validity

As explained before, we expand the coupling terms in the Hamiltonian in the fourth order in the system phases. In other words, we assume that the phase zero-point fluctuations are small, each system holds only a relatively small number of excitations, and the coupling energy is reasonably

bounded from above. We require that the inductive coupling is not in the ultrastrong regime, i.e., $g_1^j \ll \omega_a^p$. We rewrite that condition to obtain

$$\frac{E_J^c}{\tilde{E}_L^a} \ll \frac{2\varphi_{a,zpf}}{\varphi_{r,zpf}} \tag{13}$$

using the expression for g_1^j in Table I with Eqs. (5) and (8).

As already mentioned, we focus on the case of two-photon resonance, $\omega_a \approx 2\omega_r$. On the other hand, we assume that the atom single-photon transition is highly nonresonant, and we treat the linear interaction as a perturbation. The same applies to the optomechanical-type interactions in Table I. The system should not be driven in a way that induces transitions, e.g., there should be no transitions as typically used for radiative cooling and amplification [65,66].

We mentioned for Eqs. (10) that we neglect the atom self-nonlinearity induced by the coupler while calculating the rate corrections. Analogously, we neglect the resonator self-nonlinearity because it is of purely induced character (see Appendix A 3). As a result, we neglect small resonator anharmonicity in the Hamiltonian (12), as discussed in Sec. VII B. We assume that the induced nonlinearities are much weaker than the cubic nonlinearity in the atom potential. Under the condition $E_J^c \ll \tilde{E}_L^a$, we still expect a reasonable accuracy in determining the coupling rates. Also, we neglect the higher-order nonlinearities, as explained in Sec. IV A.

Finally, for calculations in Appendix B, the artificial atom possesses an infinite number of energy levels with the same anharmonicity. An analogous approximation is routinely used for the transmon artificial atom [13], with normally about ten energy levels [67] within this model. Recently, the limits of this approximation were studied for a transmon in dispersive readout [67]. In this paper, we make estimates for an rf SQUID with merely seven metastable states in Sec. VI. We further discuss the bosonic approximation in Sec. VII.

V. IMPORTANT INTERACTION DRESSING

Here we provide our analytical approximations for the resonant two-photon and cross-Kerr interactions as given in the Hamiltonian in Eq. (12), as well as for the nonresonant single-photon interaction (see notations in Table II). With diagrams, we illustrate some virtual transitions that modify the bare interaction rates.

Unlike Feynman diagrams [68,69], our diagrams are not intended for calculating the process amplitudes. As in Refs. [22,70], we show the energy states the system virtually goes through during the full interaction process. That allows us to clearly illustrate the smallest possible number of energy states for a given process to occur at all.

A. Cross-Kerr coupling due to potential asymmetry

We focus on an atom with asymmetric potential and nonlinear coupling. In that case, the cross-Kerr coupling in the effective Hamiltonian (12) is mainly corrected as

$$K_{0,X} = K_0 + \frac{24 g_2 X_a}{\omega_a^p} \tag{14}$$

$$= \frac{E_J^c}{\hbar}(\cos\delta - \mu \sin\delta)\varphi_{r,zpf}^2 \varphi_{a,zpf}^2. \tag{15}$$

TABLE II. Notations for interaction rates.

Linear interaction	
g_1^c	Bare capacitive coupling
g_1^j	Bare inductive coupling
$\tilde{g}_1^j$	Dressed inductive coupling
Nonlinear interaction	
K_0	Bare cross-Kerr coupling
$K_{0,X}$	Dressed cross-Kerr coupling
g_2	Bare two-photon coupling
	Bare optomechanical coupling
$\tilde{g}_2$	Dressed two-photon coupling
G_2	Bare two–atom-excitation coupling
	Bare reverse optomechanical coupling
J	Dressed reverse optomechanical coupling

There is no correction from the reverse optomechanical processes of rate G_2. That is the case as we neglect cubic anharmonicity in the resonator potential.

We provide the full derivation of Eq. (14) in Appendix B 1 using a Schrieffer-Wolff transformation as in Refs. [68,71]. A simpler derivation is sketched in Appendix C, where we rewrite the same transformation in a more convenient form. Appendix E gives an even more straightforward calculation based on the Heisenberg equations of motion. Following the calculation, the atom self-dressing, due to the cubic nonlinearity in its potential, spawns the cross-Kerr correction out of the optomechanical interaction of rate g_2.

In a more physical picture, the correction in Eq. (14) occurs owing to the virtual processes. The virtual optomechanical transitions of rate g_2 chain with the transitions caused by the atom nonlinearity. We illustrate some example processes in Fig. 2(a).

It is important here that two-atom processes contract into a loop. Expanding the cubic nonlinearity with energy proportional to $(b^\dagger + b)^3$, we obtain a term $bb^\dagger b = b^\dagger b^2 + [b, b^\dagger]b$. The last term here corresponds to the blue (2) process in Fig. 2(a) acting from right to left on the system state. Its Hermitian conjugate arises as the operators in the diagram act from left to right. Hence, a loop in the diagrams represents the use of the commutation relation $[b, b^\dagger] = 1$ contracting creation and annihilation operators.

The operators from the same interaction type contract as in Wick's theorem discussed in Appendix C. Such a single-colored loop only indicates the use of commutation relations to cast a bare interaction term or a Schrieffer-Wolff exponent into the normal-ordered form. In the normal order, an interaction term uses the minimal number of the energy levels while still modeling the required coupling. Hence, the single-colored loops do not require the existence of a higher-energy state. We only depict them to account for the operators "missing" after the use of commutation relations.

However, the two-color loops in Figs. 2 and 3 do require a higher-energy state. These loops arise from the $bb^\dagger$ sequence with the operators from different bare processes. We speculate in Sec. VII and Appendix C that a resulting process may not occur if the higher-energy state is not coherent enough. Then such sequences cannot be simply normal-ordered in

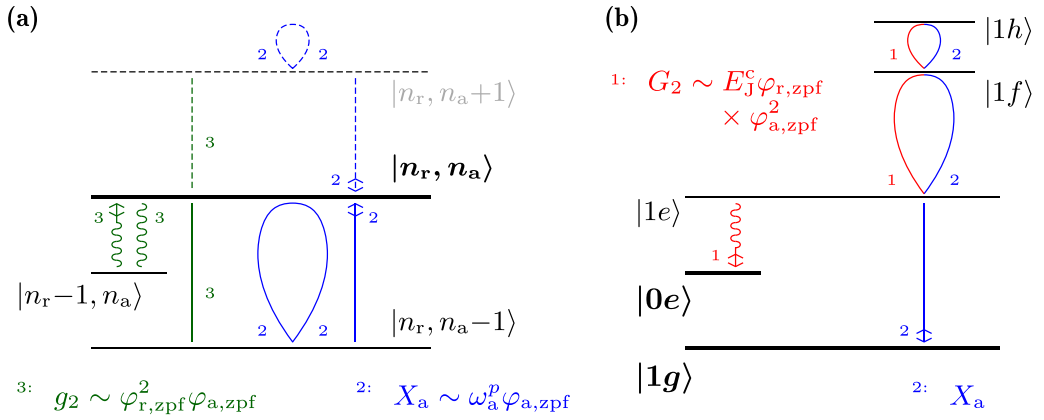


FIG. 2. Some corrections to the bare cross-Kerr and linear couplings, due to nonresonant bare processes in Table I. (a) Cross-Kerr correction due to optomechanical coupling g_2 with the energy quadratic in the resonator variables (3, green) combined with the cubic nonlinearity of the atom potential X_a (2, blue). The optomechanical matrix element $\langle n_r, n_a|g_2 a^\dagger a b^\dagger|n_r, n_a-1\rangle + \text{H.c.} \propto g_2 n_r\sqrt{n_a}$ and the atom nonlinearity matrix element $\langle n_a-1|X_a[b, b^\dagger]b|n_a\rangle \propto \sqrt{n_a}$ combine into the full process amplitude $\propto n_r n_a$. The first index in a state label denotes the number of the resonator energy level, while the second one labels the atom level. The dashed lines correspond to an alternative process path that climbs the atom energy ladder as high as possible. (b) Inductive single-photon correction due to the combination of the interaction G_2 with the energy quadratic in the atom variables (1, red) and the atom cubic nonlinearity. The full process is chosen to excite the atom as high as possible. Loops contract creation and annihilation, such that only vacuum parts contribute—i.e., the unity in $bb^\dagger = 1 + b^\dagger b$. The same-color loops do not rely on the availability of a next energy level. Each virtual process brings a relevant factor (in corresponding colors and positions) to the full amplitude. Other notations are as in Table I.

the bosonic approximation. Our argument in the appendix is based on the Schrieffer-Wolff formalism.

In the diagrams in this work, we present such processes that climb the atom energy ladder as high as possible. In Appendix D, we give a detailed recipe for determining such processes.

We only account for the cross-Kerr dressing as in Eqs. (14) and (15). Other corrections arise from the nonresonant exchange interactions as for the dispersive shift in circuit quantum electrodynamics [11–13,72,73]. Dispersive corrections from the linear interaction are about $\Xi_a g_-^2/(\omega_a - \omega_r)^2$ or less. That can be nonnegligible, but for $\omega_a \approx 2\omega_r$ they only become comparable to the main cross-Kerr correction in Eqs. (14) and (15) with high anharmonicities $|\Xi_a|/\omega_r \gtrsim |g_2 X_a|/g_-^2 \approx \mu\omega_a \sin^2\delta/|12E_J^c\cos\delta|$. This threshold value of $|\Xi_a|/\omega_r$ is large near $\delta = \pi/2$ with large two-photon coupling g_2. In addition, our preliminary calculations show that, for nonlinear coupling and asymmetry in the atom potential, there is another correction of about $\mu g_- G_2 \varphi_{a,zpf}/\omega_r$. It can also matter where the two-photon coupling is large, although it becomes comparable to the main cross-Kerr correction when $|g_-| \gtrsim |X_a|$ for $\varphi_{a,zpf} \sim \varphi_{r,zpf}$. For the estimates in Sec. VI, both dispersive corrections are small.

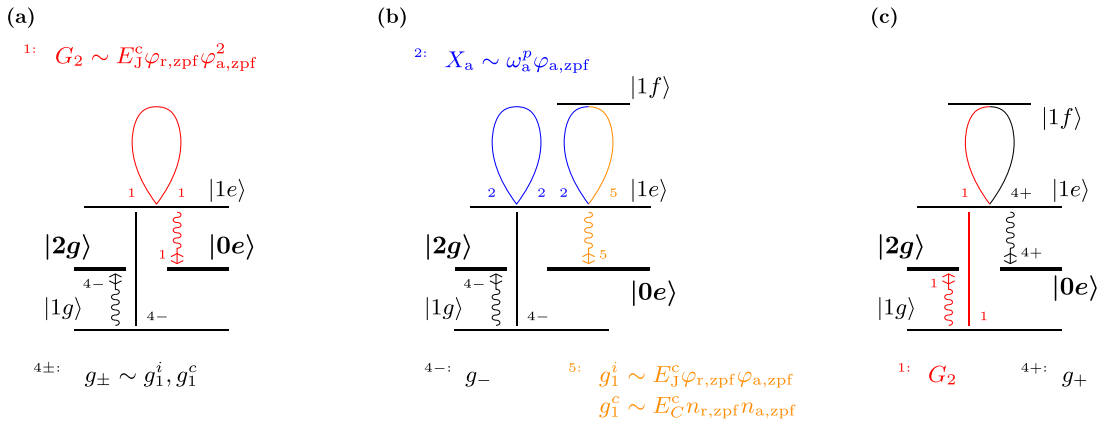


FIG. 3. Some corrections to the two-photon coupling. (a) Virtual transitions $0e \leftrightarrow 1e$ and $1e \leftrightarrow 2g$ mediated by the number-conserving linear coupling g_- (4− black) and the quadratic coupling G_2 (1, red). (b) Virtual transitions $2g \leftrightarrow 1e$ with the number-conserving linear coupling as well as $1e \leftrightarrow 0e$ with the atom cubic nonlinearity X_a (2, blue) and the number-nonconserving part of either g_1^i the linear inductive or g_1^c the linear capacitive coupling (5, orange). (c) Virtual transitions $0e \leftrightarrow 1e$ and $1e \leftrightarrow 2g$ mediated by the two–atom-excitation coupling G_2 and the number-nonconserving linear inductive interaction g_+ (4+ black). The depicted processes are chosen to excite the atom as high as possible. Other notations as in Fig. 2 and Table I.

B. Nonresonant linear interactions

While we assume that the linear interactions are strongly nonresonant, they can become relevant if the coupler is used with a multimode resonator or a waveguide. Here we discuss the dressing of the linear inductive interaction as mediated by the coupling SQUID.

According to Appendix B 2, the rate of the linear inductive interaction renormalizes as

$$\tilde{g}_1^i \approx g_1^i - \frac{20 G_2 X_\mathrm{a}}{\omega_\mathrm{a}^p} \tag{16}$$

$$= \frac{E_\mathrm{J}^\mathrm{c}}{\hbar}\left(\cos\delta - \frac{5}{6}\mu\varphi_{\mathrm{a,zpf}}^2 \sin\delta\right)\varphi_{\mathrm{r,zpf}}\varphi_{\mathrm{a,zpf}}. \tag{17}$$

We provide the dominant terms for both parts proportional to $\cos\delta$ and $\sin\delta$. The first term in Eq. (16) is the rate of bare inductive interaction due to the coupler Josephson inductance, as given in Table I. When $\delta \mod \pi = \pi/2$, this bare coupling vanishes. Hence the second term in Eq. (16) becomes dominant close to that point. Equation (17) allows us to determine the coupling regime with vanishing single-photon interactions more precisely in Sec. VI E.

As follows from the calculation in Appendix B 1, the second term in Eq. (16) arises with the dressing of the atom in the harmonic approximation by the interactions with itself. Namely, this occurs via its cubic nonlinearity as in Table I. That dressing spawns the correction to the linear coupling out of the interaction G_2 in the table.

The correction to the inductive single-photon coupling in Eqs. (16) and (17) can be understood further. It arises from the virtual transitions as the G_2 interaction chains with the transitions due to the atom nonlinearity. We illustrate two such processes in Fig. 2(b).

In the correction in Eq. (17), four atom processes contract into two loops. This allows for the required $\sqrt{m}$ coefficient when the full sequence acts on an atom excited state $\propto b^{\dagger m}|g\rangle$. Moreover, in Fig. 2(b), we put the loops one above the other. They correspond to the vacuum part of the $b^2 b^{\dagger 2}$ process when reading the diagram from right to left. Note also how operators from different interactions can contribute to a loop. In that case, an additional energy level is required for the loop to form, as discussed in Appendix C.

In our model, there are no corrections to the capacitive single-photon coupling as in Table I. The reason is that both the atom nonlinearity and the quadratic couplings in Table I are of the inductive type alone, i.e., they depend only on the atom phase variable $\propto (b^\dagger + b)$. When combined, they only result in inductive interactions.

C. Two-photon coupling

We find that the corrections to the two-photon coupling are typically small. We point out these corrections and argue that the two-photon coupling in the Hamiltonian (12) can be approximated with its bare value as $\tilde{g}_2 \approx g_2$.

Recall that we consider bare interactions from the fourth-order expansion of the Josephson coupling energy. The two-photon processes contain an odd number of creation and annihilation operators. Therefore, a correction process involves either the G_2 process or the X_a atom self-nonlinearity process. The lowest-order process with G_2 also requires a linear interaction as in Figs. 3(a) and 3(c). The process with X_a requires two linear interactions as in Fig. 3(b). These process amplitudes are of the fifth order in the zero-point fluctuations.

However, these processes can be nonnegligible in our fourth-order expansion of the coupling. The next-order expansion term adds $(g_2/2)(\varphi_{\mathrm{r,zpf}}^2 + \varphi_{\mathrm{a,zpf}}^2)$ to the bare rate. Consider the purely inductive corrections in Fig. 3 of about $(E_\mathrm{J}^\mathrm{c}/\hbar)^2\varphi_{\mathrm{r,zpf}}^2\varphi_{\mathrm{a,zpf}}^3/\omega_\mathrm{r}$, where the denominator takes into account the nonresonant character of the process parts. For a stronger Josephson coupling energy E_J^c, these corrections can exceed the neglected fifth-order expansion term linear in E_J^c. That is the case when

$$4E_\mathrm{J}^\mathrm{c} \gg \hbar\omega_\mathrm{r}\left(1 + \varphi_{\mathrm{r,zpf}}^2\varphi_{\mathrm{a,zpf}}^{-2}\right). \tag{18}$$

We explicitly provide these two-photon rate corrections and discuss them in detail in Appendix F 2.

Still, the two-photon corrections are small compared with the bare coupling g_2 under reasonable assumptions. Amplitudes of the corrections in Figs. 3(a) and 3(c) are proportional to $g_\pm G_2/\omega_\mathrm{r}$. However, $g_\pm \ll \omega_\mathrm{r}$ as we require the coupling strength below the ultrastrong regime. On the other hand, $G_2 \sim g_2$, according to Table I, once the resonator and the atom zero-point fluctuations are of the same order of magnitude, $\varphi_{\mathrm{r,zpf}} \sim \varphi_{\mathrm{a,zpf}}$. In the other case with $\varphi_{\mathrm{r,zpf}} \ll \varphi_{\mathrm{a,zpf}}$, the corrections like in Figs. 3(a) and 3(c) can be of the same order as the bare two-photon coupling.

The correction with X_a as in Fig. 3(b) arises even in the absence of nonlinear coupling. However, it is even smaller than the other corrections, according to the expressions in Appendix F 2. A similar process yields two-photon coupling with the rate $2\mu g_+ g_1^c \varphi_{\mathrm{a,zpf}}/9\omega_\mathrm{r}$. It involves capacitive coupling g_1^c instead of the inductive g_1^i in Fig. 3(b). In principle, it can be arbitrarily strong; however, for arranging two-photon coupling it makes sense to limit $g_1^c \sim g_1^i$ as discussed in Appendix F 2.

VI. NUMERICAL ESTIMATES

In this section, we use our analytical results to calculate the coupling rates and their dressing. As in the preceding part [20], we consider the artificial atom to dwell in its metastable well initially. We tune the well to accommodate more than enough metastable states to sustain the dressing virtual transitions in Figs. 2 and 3. At the same time, we seek the atom anharmonicity to be much stronger than the two-photon interaction rate. This regime resembles the phase qubit in Ref. [74].

Also, we explain how we match the lowest two-photon resonance, i.e., for the $0e \leftrightarrow 2g$ transition. We focus on the case of strong coupling, where the two-photon coupling rate $\tilde{g}_2$ exceeds the damping rates. Hence, we consider the systems to be resonant when their detuning is below $\tilde{g}_2$, analogously to the results of Ref. [75] for the single-photon coupling.

A. Phase qubit regime of the rf SQUID

The exact expression for the isolated rf SQUID potential energy reads

$$U_\mathrm{a} = \frac{E_L^\mathrm{a}}{2}\left(\phi_\mathrm{a} - \frac{2\pi\Phi_\mathrm{e}}{\Phi_0}\right)^2 - E_\mathrm{J}^\mathrm{a}\cos\phi_\mathrm{a}. \tag{19}$$

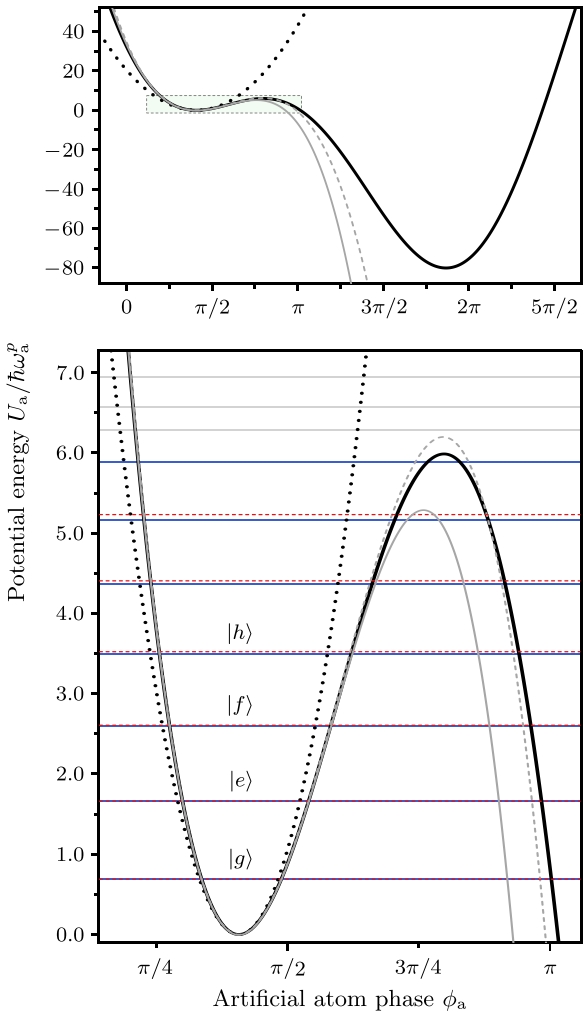


FIG. 4. (top panel) Double-well potential (thick black) of the uncoupled rf SQUID as given by Eq. (19). Other curves show the potential in the harmonic (dotted), cubic (thin dashed), and quartic (thin solid) approximations. The energy origin is at the bottom of the left well. The shaded rectangle highlights the region shown in the other panel. (bottom panel) Metastable well hosting levels $|g\rangle$, $|e\rangle$, $|f\rangle$, $|h\rangle$, and three others. Solid lines indicate the energies of metastable states and several over-the-barrier states, selected among numerical solutions of the stationary Schrödinger equation for the full potential. Dashed lines indicate the energy levels according to the perturbation theory as in Eq. (20). Atom parameters: ratio of the capacitive and inductive energies $E_C^a/E_L^a = 3.950 \times 10^{-4}$, screening parameter $\beta_L = E_J^a/E_L^a = 3.3424$, and external flux $\Phi_e = 0.7150\Phi_0$.

The potential and energy levels are shown in Fig. 4 for the uncoupled rf SQUID. Turning on the Josephson coupling only renormalizes the atom Josephson inductance. According to Eq. (4b), this distorts the potential only slightly when $E_J^c \ll E_L^a + E_J^a \cos\phi_a^{\min}$. For the energy ratios and external flux as in the Fig. 4 caption, the atom equilibrium phase is $\phi_a^{\min} \approx 0.4091\pi$. Hence the atom Josephson energy improves the criterion by about $E_J^a \cos\phi_a^{\min} \approx 0.9411 E_L^a$.

Here and in Sec. VI C, we first provide the energies and frequencies for the isolated systems. That is, $E_J^c = 0$ both for determining the inductive energies in Eqs. (4) and the equilibria in Appendix A 2, while $C_c' = 0$ for determining the capacitive energies.

We choose the rf SQUID inductance $L_a = 1.0000$ nH ($E_L^a/h = 163.46$ GHz) and critical current $I_0^a = 1.1000$ μA ($E_J^a/h = 546.35$ GHz) close to Ref. [34]. However, we pick a smaller full capacitance of the artificial atom $C_a' = 300.0$ fF ($E_C^a/h = 64.57$ MHz) to increase its anharmonicity. The rf SQUID external flux is indicated in the Fig. 4 caption. These parameters yield the plasma frequency of the metastable well $\omega_a^p = 2\pi \times 12.80$ GHz and the magnitudes of zero-point fluctuations $n_{a,zpf} = 3.520$ and $\varphi_{a,zpf} = 0.1420$.

Anharmonicity in the metastable well is $[(E_e - E_g) - (E_f - E_e)]/h = 391.28$ MHz, where E_g, E_e, and E_f are the eigenenergies from the numerical solution of the Schrödinger equation. On the other hand, the perturbative estimate with Eq. (21) yields $\Xi_a = 2\pi \times 325.04$ MHz. In the phase qubit regime, the main contribution to the anharmonicity arises from the cubic nonlinearity in the atom potential, as we detail below in Sec. VI C.

Note that, for the capacitance density of 50 fF/μm^2 in a Josephson junction and its critical current density of 1.7 μA/μm^2 [15,76], the self-capacitance of the atom junction is about 32 fF for our choice of the critical current I_0^a. Thus, to achieve the total capacitance of the rf SQUID as above, one needs a 170 fF shunting capacitance.

Notice how the perturbative energy levels in Fig. 4 compare with the levels calculated numerically. The perturbative results there are according to the second-quantized Hamiltonian (B4) in Appendix B. Discrepancies with the numerics are only visible close to the barrier top. They occur as the potential nonlinearities become comparable to its harmonic approximation. For the highest metastable level, the well becomes visibly wider than the harmonic approximation. At the same time, the barrier becomes so thin that the wave functions should spread into it much deeper. Hence the energies are below the perturbation theory result, as seen in the figure.

Moreover, the perturbative theory misses one metastable level altogether. We calculate the perturbative energy levels for the fourth-order approximation to the potential. It breaks down vividly near the barrier top (see Fig. 4) and hence misses one metastable level. Note that the cubic approximation happens to work better near the barrier top. However, we use the fourth-order one, as we are more interested in predicting the lowest transition frequency analytically.

B. Coupler parameters

We choose a moderate value of the coupler Josephson energy. Each of its junctions with critical current $I_0^c = 30$ nA possesses the energy of $E_{1J}^c/h \approx 14.90$ GHz. With capacitance $C_c' = 5$ fF ($E_C^c/h \approx 2.70$ MHz), the coupler mediates a capacitive coupling with a rate of about $2\pi \times 50$ MHz, well-attainable in circuit quantum electrodynamics [63,77].

We consider the coupler Josephson energy that is relatively small compared with other respective energies that are relevant for determining the transition frequencies, $2E_{1J}^c \approx 0.1(E_L^a + E_J^a \cos\phi_a^{\min})$, $0.1E_L^r$. Still, variation of this coupler energy may bring the system off-resonance. Indeed, $2E_{1J}^c$ shifts both the atom and the resonator full inductive energies as in Eqs. (4). Depending on the coupler bias Φ_c, that

yields a variation in the detuning $\omega_a - 2\omega_r \sim \omega_a^p - 2\omega_r^p$ of up to about $E_{1J}^c|\omega_a^p/E_J^a - 2\omega_r^p/E_L^r| \approx 0.1\omega_a^p$. Under normal circumstances, this far exceeds both the linewidths and the two-photon coupling rate $\tilde{g}_2$. That said, we aim for the resonance to occur close to the coupler bias with the highest two-photon coupling rate $\tilde{g}_2$.

C. Resonator parameters and analytics for the resonance position

We choose the resonator parameters to hit the resonance as described below. In addition, we fix the resonator and atom zero-point phase fluctuations to have close amplitudes. We arrive at the resonator inductance $L_r = 0.84868$ nH ($E_L^r/h = 192.61$ GHz) and capacitance $C_r = 692.8$ fF ($E_C^r/h = 27.05$ MHz). For an uncoupled resonator, this yields plasma frequency $\omega_r^p = 2\pi \times 6.56$ GHz and zero-point fluctuations with amplitudes $n_{r,zpf} = 3.830$ and $\varphi_{r,zpf} = 0.1305$.

One may expect that the two-photon coupling rate $\tilde{g}_2$ is close to its maximum when the inductive component of the coupling is fully turned on with $E_J^c = 2E_{1J}^c$. According to Eq. (1), the latter occurs at zero coupler bias, $\Phi_c = 0$. On the other hand, the main contribution to $\tilde{g}_2$ arises from its bare part g_2, which maximizes for $\delta \mod \pi = \pi/2$. As the coupler static phase δ depends on Φ_c as in Eq. (2), these simple conditions do not necessarily coincide. However, we rely on the rf SQUID static phase $\phi_a^{\min}$ to provide most of the required coupler phase δ. This assumption holds relatively well for the atom as in Sec. VI A (see also Fig. 4). Hence, leaving $\Phi_c = 0$ indeed yields reasonably high values of $\tilde{g}_2$ with such a value of $\phi_a^{\min}$.

Therefore, we choose the resonator parameters above so that the two-photon resonance occurs for $\phi_a^{\min}$ as in Sec. VI A and zero coupler bias, $\Phi_c = 0$. Additionally, with such a choice, our results are directly applicable for a single-junction coupler as discussed in Sec. VI E.

In the rest of Sec. VI C, we verify the resonance condition with an analytical approximation. We approximate the frequencies in the Hamiltonian (12) as

$$\omega_r \approx \omega_r^p - \frac{K_{0,X}}{2}, \quad \omega_a \approx \omega_a^p - \Xi_a - \frac{K_{0,X}}{2}. \tag{20}$$

Here we omit other interaction-induced shifts that are of order of $g_\pm^2/\omega_{r,a}$ and $\Xi_a g_\pm^2/\omega_{r,a}^2$ or smaller. We report in Sec. V A that $K_{0,X}$ in Eqs. (20) is also the main contribution to the cross-Kerr coupling strength. Another frequency shift is of the same magnitude as the atom anharmonicity

$$\Xi_a = \frac{E_C^a}{\hbar}\left[\frac{5}{3}\left(\frac{E_L^a}{\tilde{E}_L^a}\right)^2\left(\phi_a^{\min} - \frac{2\pi\Phi_e}{\Phi_0}\right)^2 - \frac{E_L^a - \tilde{E}_L^a}{\tilde{E}_L^a}\right]. \tag{21}$$

It arises from the same self-nonlinearities as the anharmonicity. In the brackets in Eq. (21), the first term comes from the cubic perturbation in the atom potential. The second one is the quartic correction. See Appendix B for a derivation using the Schrieffer-Wolff transformations. Note that the shift analogous to Ξ_a is negligibly small in the resonator frequency, ω_r as we discuss in Sec. VII B.

According to Eqs. (20), the resonator and the atom frequencies are $\omega_r \approx 2\pi \times 6.74$ GHz $- K_{0,X}/2$ and $\omega_a \approx 2\pi \times 13.49$ GHz $- K_{0,X}/2$. It is already clear that we hit the resonance when $K_{0,X}/2 < \tilde{g}_2$. In fact, calculations yield $K_{0,X} \approx 2\pi \times 15.7$ MHz and $|\omega_a - 2\omega_r| \approx 2\pi \times 1.5$ MHz while $\tilde{g}_2 \approx 2\pi \times 27.0$ MHz.

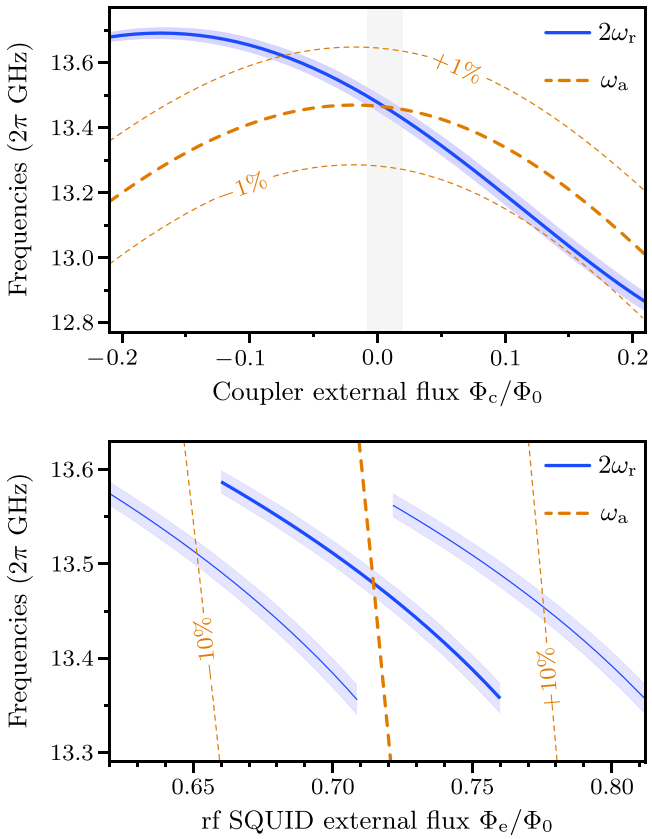


FIG. 5. Dependence of the resonator and atom frequencies on the flux biases: the coupler bias Φ_c in the upper panel and the atom bias Φ_e in the lower panel. Resonator frequency ω_r according to Eq. (20); atom frequency ω_a determined numerically as described in the text. The blue area is the region from $2\omega_r - \tilde{g}_2$ to $2\omega_r + \tilde{g}_2$, where $\tilde{g}_2$ is the two-photon coupling strength. Gray shade marks the minimal region of the $0e \leftrightarrow 2g$ resonance, i.e., where the detuning is smaller than $\tilde{g}_2$. Circuit parameters are as in the text. Thin lines show the frequencies when the atom Josephson energy E_J^a departs from the required value by the indicated fraction.

Note also that the quartic contribution to the anharmonicity in Eq. (21) provides a correction of order of magnitude of $E_C^a/\hbar$. More precisely, it is about 30 MHz with the artificial atom parameters as in Sec. VI A. This correction exceeds $\tilde{g}_2$ and hence is important for us. The same holds for the contribution of about 10% in Ξ_a due to the coupler Josephson inductance.

D. Numerics for the resonance position

Furthermore, we study the resonance position numerically in Fig. 5. It demonstrates how the system frequencies depend on the coupler bias Φ_c and the atom bias Φ_e. Near the curve intersections, the two-photon transition $0e \leftrightarrow 2g$ is resonant. To determine the atom frequency in the figure, we solve the

Schrödinger equation for the rf SQUID potential [20]

$$U'_{\rm a} = U_{\rm a} - E_{\rm J}^{\rm c}\cos\left(\phi_{\rm r}^{\rm min} - \phi_{\rm a} - \frac{\pi\Phi_{\rm c}}{\Phi_0}\right) \tag{22}$$

that is perturbed by the coupler. Here the potential $U_{\rm a}$ of the uncoupled atom is given by Eq. (19). For each value of the bias $\Phi_{\rm c}$, we determine $\phi_{\rm r}^{\rm min}$ and $\phi_{\rm a}^{\rm min}$ from the equations for equilibrium in Appendix A 2, before solving the Schrödinger equation.

The upper panel in Fig. 5 supports our analytical estimates. For $\Phi_{\rm c} = 0$, the atom frequency is $\omega_{\rm a} \approx 2\pi \times 13.47$ GHz $- K_{0,X}/2$. That differs from the analytical prediction by about $2\pi \times 10$ MHz. Mostly, this error arises because the analytics underestimates the atom anharmonicity (see Sec. VI A). We have verified that, for a smaller number of metastable energy levels, this discrepancy increases.

A more fundamental discrepancy occurs with the variation of the atom Josephson energy $E_{\rm J}^{\rm a}$. It is caused by fabrication imperfections, primarily fluctuations of the junction area and inhomogeneities in the insulating barrier [78–80]. Figure 5 also shows how sensitive the resonance is to the variation of $E_{\rm J}^{\rm a}$.

In any case, we expect that one can recover the resonance by tuning the atom transition frequency. It can be varied in a rather wide range *in situ* by changing the atom bias $\Phi_{\rm e}$. According to the lower panel of Fig. 5, a bias shift of $\pm 0.06\Phi_0$ mitigates the detuning arising from the $\pm 10\%$ deviation in $E_{\rm J}^{\rm a}$. Note that modern fabrication techniques [78,81] keep the Josephson energy variations well below 10%.

A change in $E_{\rm J}^{\rm a}$ also shifts the resonator frequency $\omega_{\rm r}$ as shown in the Fig. 5 lower panel. That occurs as the atom equilibrium $\phi_{\rm a}^{\rm min}$ shifts (see the equations in Appendix A 2), which changes the coupler static phase difference δ. In turn, this alters the magnitude of the coupler Josephson inductance that loads the resonator [see Eq. (4a)]. A similar contribution is present in the $\omega_{\rm a}$ shift. It arises due to the direct change of $E_{\rm J}^{\rm a}$ in Eqs. (4b) and (5) combined with the associated change in $\phi_{\rm a}^{\rm min}$.

E. Interactions

Figure 6 demonstrates how the interaction rates in Table II depend on the coupler external flux $\Phi_{\rm c}$. In addition to the trivial modulation of the coupler Josephson energy, $\Phi_{\rm c}$ also alters the symmetry of the Josephson interaction. That is, it regulates the onset of the odd components in the coupling energy, including the two-photon interaction. For each value of $\Phi_{\rm c}$ in the plots, we numerically solve the equations for the equilibrium point in Appendix A 2 to obtain $\phi_{\rm r}^{\rm min}$ and $\phi_{\rm a}^{\rm min}$.

The top panel in Fig. 6 shows the full single-photon coupling rate $\tilde{g}_- = g_1^c - \tilde{g}_1^i$ along with the two contributions that constitute it: the capacitive coupling g_1^c as in Table I and the full inductive coupling $\tilde{g}_1^i$ as in Eq. (17). We also plot the bare inductive coupling g_1^i as in Table I. Notice that the capacitive coupling is virtually constant in the coupler bias. That is to be expected, as renormalizations due to the coupler Josephson inductance in Eqs. (4a) and (4b) are negligible for $E_{\rm J}^{\rm c} \ll E_L^{\rm r}, E_L^{\rm a}$.

By setting $\Phi_{\rm c} \mod \Phi_0 = \Phi_0/2$, we turn off the coupler Josephson energy, $E_{\rm J}^{\rm c} = 0$. Thus, all linear and nonlinear inductive-type couplings vanish, leaving only the capacitive coupling. On the other hand, the bare inductive coupling g_1^i vanishes as $\Phi_{\rm c}$ satisfies $\delta \mod \pi = \pi/2$, where δ is given by Eq. (2).

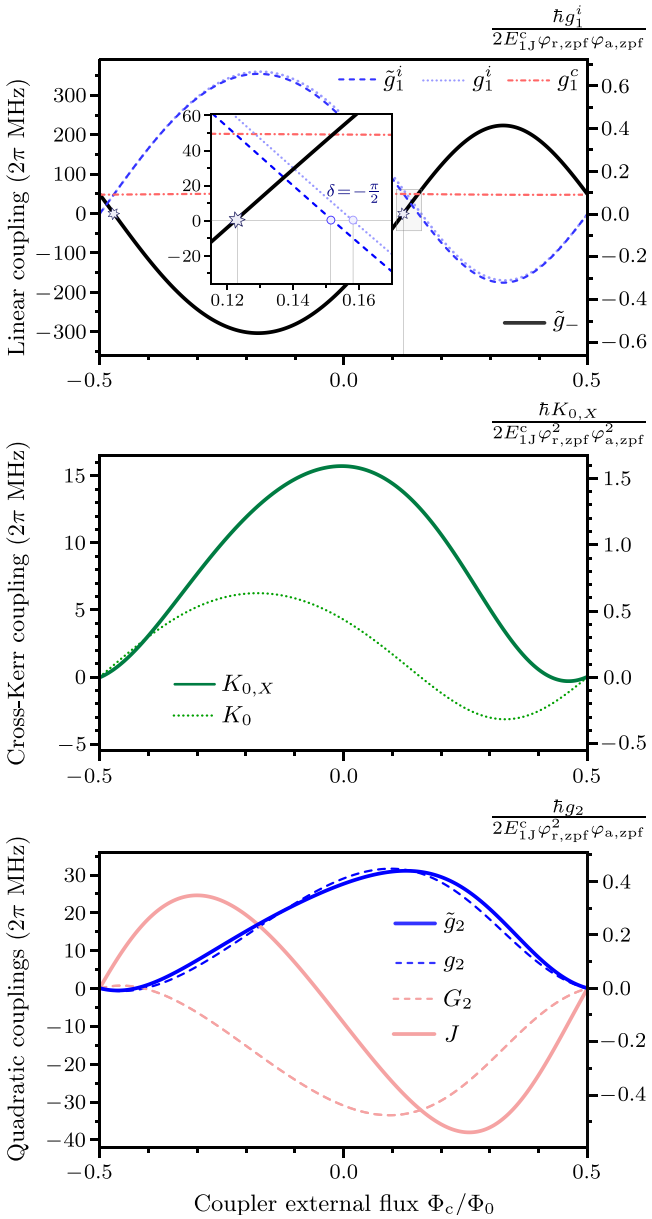


FIG. 6. Dependence of the interaction rates on the coupler bias $\Phi_{\rm c}$, as expressed in Table I, Sec. V, and Appendix F. (Linear coupling): Total inductive $\tilde{g}_1^i$, bare inductive and capacitive g_1^i and g_1^c, total excitation-number–preserving $\tilde{g}_- = g_1^c - \tilde{g}_1^i$. The inset shows the vicinity of $\Phi_{\rm c}$ where either g_1^i or $\tilde{g}_1^i$ become zero (circles). Stars mark the biases where g_- vanishes. (Cross-Kerr coupling): $K_{0,X}$ [Eq. (15)] with the asymmetry-induced correction, bare K_0. (Quadratic couplings): Full reverse optomechanical J, two-photon bare g_2, full two-photon $\tilde{g}_2$. The coupling quadratic in the artificial atom phase has the rate G_2. rf SQUID regime as in Fig. 4. Dimensionless axes neglect the dependence of the zero-point amplitudes of the resonator and atom, $\varphi_{\rm r,zpf}$ and $\varphi_{\rm a,zpf}$, on the coupler Josephson energy as it varies with $\Phi_{\rm c}$. The maximal magnitude of the coupler Josephson energy is denoted by $2E_{1\rm J}$.

The full inductive coupling $\tilde{g}_1^j$ has an additional component due to the asymmetry in the atom potential. With the cubic nonlinearity coefficient $\mu = 1.651$ (for $E_J^c = 0$ and $C_c' = 0$), this component is noticeable in the plot as a difference between $\tilde{g}_1^j$ and g_1^j. As follows from Eq. (17), $\tilde{g}_1^j$ vanishes for the bias determined by the condition $\cot\delta = \frac{5}{6}\mu\varphi_{a,zpf}^2$. The zero-shifting component $\tilde{g}_i - g_i$ is proportional to the bare G_2 interaction (see lower panel) and $\sin\delta$. Hence, this component is close to its maximal magnitude right near the zero of the bare coupling g_1^j. The expression for the full rate $\tilde{g}_-$ suggests an important property: for specific values of the external flux Φ_c, the capacitive and inductive couplings cancel each other out, and the single-photon coupling switches off [52,82–84]. We mark these values of Φ_c in Fig. 6.

The middle panel in Fig. 6 demonstrates the cross-Kerr coupling rate $K_{0,X}$ as in Eq. (15) that takes into account virtual processes due to the atom cubic nonlinearity. We also plot the bare rate K_0 as in Table I; as follows from the equation, it vanishes for Φ_c at either $\delta \mod \pi = \pi/2$ or $\Phi_c \mod \Phi_0 = \Phi_0/2$, analogously to the inductive coupling g_1^j.

Note that we do not tune the resonance for every Φ_c. According to Fig. 5, the two-photon coupling becomes off-resonant further away from $\Phi_c = 0$. Hence, an additional cross-Kerr coupling arises. However, it is as small as the other dispersive couplings neglected in Sec. V A.

The bottom panel in Fig. 6 shows the couplings with the energy quadratic in the atom variables, particularly the sought-after two-photon coupling. The bare two-photon coupling g_2 dominates the corrections in $\tilde{g}_2$, as provided in Appendix F 2 and illustrated in Fig. 3. As in the cross-Kerr coupling rate, the corrections are more pronounced with higher linear coupling strength $g_\pm$. Close to the maximal magnitude of the two-photon coupling, $\tilde{g}_\pm$ is vanishing and the two-photon corrections in Appendix F 2 are not even visible.

This implies that the maximal strength of the two-photon coupling $\tilde{g}_2$ depends roughly linearly on the coupling energy E_J^c according to Table I. On the other hand, the value of E_J^c is bounded by the condition (13). When it does not hold, our perturbative treatment of the off-resonant single-photon coupling breaks down.

Note that, for the unbiased coupling SQUID, when $\Phi_c = 0$, the magnitude of the two-photon coupling is only about 11% smaller than at its maximum. Hence, if that is a reasonable trade-off, a single Josephson junction may be used instead of a coupling SQUID, possibly reducing the amount of noise in the system. In that case, two-photon coupling arises solely due to a nonzero equilibrium phase of the metastable rf SQUID, as discussed in the preceding work [20].

VII. DISCUSSION

Here we discuss the bosonic approximation, neglecting some nonlinearities, coupling to the environment, and whether our corrections are quantum.

A. Commutation relations for the atom operators

1. Bosonic approximation

In determining the corrections, we rely on the bosonic approximation for the artificial atom metastable states. In other words, we assume that the atom does not leave its metastable well as in Fig. 4, while, at the same time, it can be excited arbitrarily high in energy. Clearly, these two assumptions are contradictory for a metastable potential. However, we expect them to hold for the atom phase dwelling sufficiently close to the metastable well minimum.

More precisely, we assess the plausibility of the bosonic approximation by looking into the virtual processes that comprise the corrections. We found that the main cross-Kerr renormalization in Eq. (15) requires at least three coherent energy states, as shown for a contributing virtual process in Fig. 2(a). Other less important corrections require at most four coherent energy states to be available: See Fig. 2(b) for a single-photon $(n+1)g \leftrightarrow ne$ correction, as in Eqs. (16) and (17), and Fig. 3(b) for a two-photon $(n+2)g \leftrightarrow ne$ correction, as in Appendix F 2.

All mentioned processes occur well within the seven metastable energy states of the rf SQUID in Sec. VI. On the other hand, a process going beyond that occurs differently than predicted by the bosonic approximation. Such a real process can bring the system out of the metastable state subspace as the rf SQUID relaxes into the right well in Fig. 4. At the same time, a virtual process as predicted by the bosonic model may not occur in that case—if the dissipation into the right well is too fast.

2. Quasispin approximation as an alternative

Another approach is to cut the Hilbert space to the metastable states early [22,23]. In this model, processes that excite the atom to the over-the-barrier energy states are not allowed; algebraically, for example, that corresponds to $\sigma_+|u\rangle = 0$ for a system with the highest energy state $|u\rangle$, where the raising operator acts as $\sigma_+|g\rangle = |e\rangle$, etc. This model predicts that a real process going above the metastable levels does not occur, although in reality the system can leave the metastable subspace in that case. However, for the calculation of renormalizations due to virtual processes, the quasispin approximation may be a better model because it takes into account only the processes within the quasispin subspace. This restriction from above is encoded into the commutation relations $[\sigma_+, \sigma_-] = Z$. Here $\sigma_+ = (X + Y)/2$ and $\sigma_- = (X - Y)/2$ are the raising and lowering operators, where $\hbar X/2$, $\hbar Y/2$, and $\hbar Z/2$ are the quasispin projection operators for the respective axes. In other words, in $\sigma_-\sigma_+ = \sigma_+\sigma_- - Z$, the state-dependent addition Z on the right-hand side ensures that it vanishes when acting on the highest excited state $|u\rangle$.

We only mention here that our Schrieffer-Wolff calculations in Appendix B would be even more tedious in the quasispin approximation, where the commutator of the ladder operators is operator-valued. As for determining the best model to describe the metastable energy states, we leave that for future work. A similar question arises for modeling transmons that can "ionize" due to energetic driving [67,85]. Even putting the ionization aside, transmons are typically modeled analytically as anharmonic oscillators [4,6,13], and numerically as three-level systems [29].

3. Seminumerical estimate for the cross-Kerr rate

As a confirmation of the analytical description with bosonic operators, we perform a seminumerical estimate. Consider the atom in the first-excited state $|e\rangle$ in the metastable well. We approximate the cross-Kerr coupling rate in the effective Hamiltonian (12) as

$$K_{0,X} \approx \tfrac{1}{2}K_0\varphi_{\mathrm{a,zpf}}^{-2}\big(\langle e|\varphi_{\mathrm{a}}^2|e\rangle - \langle g|\varphi_{\mathrm{a}}^2|g\rangle\big) + 2g_2\varphi_{\mathrm{a,zpf}}^{-1}(\langle e|\varphi_{\mathrm{a}}|e\rangle - \langle g|\varphi_{\mathrm{a}}|g\rangle), \tag{23}$$

which follows from the expansion of the coupling energy to the fourth order and finding the diagonal matrix elements of the atom. The second term here is nonzero when the atom potential is asymmetrical, and hence its wave functions are not even or odd in the phase. On the other hand, the first term equals K_0 for the purely linear oscillator. In this approach, the atom anharmonicity is accounted for via its matrix elements and wave functions.

Using the numerical solution of the Schrödinger equation for the atom to calculate the matrix elements in Eq. (23), we estimate $K_{0,X} \approx 2\pi \times 17.0$ MHz for $\Phi_{\mathrm{c}} = 0$ and other parameters as in Sec. VI. According to our analytical estimate, $K_{0,X} \approx 2\pi \times 15.7$ MHz as in Fig. 6. Note that the deviation between the first term in Eq. (23) and K_0 is $2\pi \times 338$ kHz. We have verified that the overall difference with the analytical $K_{0,X}$ drops to about 2% for a configuration with 32 metastable states.

4. Two-photon coupling

As argued in Sec. V C, the main part of the two-photon coupling rate $\tilde{g}_2$ typically comes from the bare interaction g_2. That is the case for reasonable linear coupling rates and comparable zero-point fluctuations of the atom and resonator. We have also demonstrated that in the estimates of Sec. VI. That confirms our assumption in the preceding work [20], where we claimed it is enough to assess the bare two-photon coupling. Moreover, that suggests that our estimate for attainable magnitudes of the two-photon coupling does not rely on the bosonic approximation.

B. Neglected resonator anharmonicity

In tuning the resonance in Secs. VI C and VI D, we neglect the shift Ξ_{r} in the resonator frequency, which is of the same magnitude as the induced resonator anharmonicity with the energy $(-\Xi_{\mathrm{r}}/2)a^{\dagger 2}a^2$. This resonator anharmonicity (self-Kerr nonlinearity) arises due to the coupler nonlinear Josephson inductance parallel to the resonator inductance. Note that the resonator anharmonicity also dresses owing to the nonlinear interactions. Since this part does not enter the population-independent frequency shift, we are not interested in it in this work.

First, let us assess the anharmonicity magnitude for $\Phi_{\mathrm{c}} = 0$, i.e., close to the maximal values of the two-photon coupling. According to Appendix B 1, the bare part of the resonator anharmonicity is $\Xi_{\mathrm{r}} \approx \Xi_{\mathrm{r3}} + \Xi_{\mathrm{r4}}$ with $\Xi_{\mathrm{r3}} = 60X_{\mathrm{r}}^2/\omega_{\mathrm{r}}^p$ and $\Xi_{\mathrm{r4}} = 12Y_{\mathrm{r}}$. The latter denote the contributions from the cubic and the quartic parts of the resonator potential. The potential is written in Appendix A. Using the expressions therein, we calculate $X_{\mathrm{r}}/(\cos\frac{\pi\Phi_{\mathrm{c}}}{\Phi_0}\sin\delta) \approx 2\pi \times 11$ MHz and $Y_{\mathrm{r}}/(\cos\frac{\pi\Phi_{\mathrm{c}}}{\Phi_0}\cos\delta) \approx 2\pi \times 0.36$ MHz with the parameters from Sec. VI. Then, approximating $\delta \approx -\phi_{\mathrm{a}}^{\min} - \pi\Phi_{\mathrm{c}}/\Phi_0$, we obtain $\Xi_{\mathrm{r3}} \approx 2\pi \times 1.0$ MHz and $\Xi_{\mathrm{r4}} \approx 2\pi \times 1.2$ MHz for $\Phi_{\mathrm{c}} = 0$.

In fact, we find that the condition $\Xi_{\mathrm{r}} < g_2$ qualifies when $(g_2)_{\delta=\pi/2} < \frac{3\omega_{\mathrm{a}}}{20\sin\delta}(\frac{\varphi_{\mathrm{a,zpf}}^2}{\varphi_{\mathrm{r,zpf}}^2} + \varphi_{\mathrm{a,zpf}}\cot\delta)$. Hence, we expect the two-photon resonance to be unaffected by the induced resonator anharmonicity under normal conditions. Namely, that is the case below the ultrastrong coupling threshold, as in Eq. (13), as long as $\varphi_{\mathrm{a,zpf}}^2/\varphi_{\mathrm{r,zpf}}^2 \gtrsim 1$.

C. Other effects of the coupling SQUID

At first glance, the Josephson energy $E_{\mathrm{J}}^{\mathrm{c}}$ of the coupler only gives rise to inductive interactions with strengths proportional to $E_{\mathrm{J}}^{\mathrm{c}}$. Unlike the preceding part of this work [20], we take into account how $E_{\mathrm{J}}^{\mathrm{c}}$ influences other system parameters.

First of all, the coupler Josephson inductance loads the inductances of the resonator and atom. That shifts the transition frequencies as in Secs. VI B and VI C. It also alters the anharmonicities as in Secs. VI C and VII B.

The coupling rates also depend on $E_{\mathrm{J}}^{\mathrm{c}}$ via the magnitudes of the zero-point fluctuations. For $10E_{\mathrm{J}}^{\mathrm{c}} \sim E_L^{\mathrm{r}}, E_L^{\mathrm{a}}, E_{\mathrm{J}}^{\mathrm{a}}$, the variation in a coupling of order n in the zero-point fluctuations can be up to $(n/4) \times 10\%$ according to Eqs. (7), (8), and (17).

This also shifts the maximum of the two-photon coupling in Fig. 6. In addition, the maximum is influenced by the related shift of the equilibrium point. As follows from the equilibrium equations in Appendix A 2, an additional current through the coupler shifts its static phase δ depending on the bias Φ_{c}. We calculate (results not presented) that this variation in δ is about 0.1π for the parameters as in Sec. VI. That may be further analyzed in future work, along the lines of Refs. [86,87].

D. Expansion of the Josephson coupling energy

It is possible to find the coefficients for the Hamiltonian terms as in Appendix A 3 and higher in all orders of the coupling energy expansion [88–90]. However, we resort to the fourth-order expansion in our starting Hamiltonian. The reason is that we work with a relatively strong Josephson coupling to boost the two-photon processes. Consider the perturbative two-photon corrections in Appendix F 2. They are of the same order in the small zero-point fluctuations as the neglected higher-order expansion terms in the coupler energy. However, with stronger Josephson coupling, these corrections exceed the higher-order expansion terms and should be accounted for. With the relatively strong Josephson coupling, we need to tackle even higher perturbative corrections as we include the higher expansion terms. That is beyond the scope of this work.

E. Coupling to environment

If both the resonator and the artificial atom couple to the same or correlated heat baths, an additional linear coupling arises [91,92]. That influences the small two-photon rate dressing. Indeed, the latter depends on the linear coupling rate, as shown in Fig. 3 and Appendix F 2. However, such

contributions are small in the strong-coupling regime, where the interactions are faster than the dissipation.

F. Quantumness

Mathematically, the loops in Figs. 2 and 3 arise from the commutation relations between the operators. Therefore, it may seem that every correction there is a quantum effect—since each of them contains a loop.

However, that is not the case for the corrections with a single loop. We demonstrate this for the main cross-Kerr correction by obtaining it from the dynamical equations in Appendix E. This derivation is valid in the classical limit with the complex phasors [93,94] instead of the operators a and b. Hence, our single-loop corrections are also present in the classical systems.

Roughly speaking, one loop in the diagrams and the corresponding commutator arise as the Schrieffer-Wolff transformation takes into account a part of the system dynamics. Similarly to the commutators we use to obtain the Heisenberg equations of motion from a Hamiltonian, the corresponding commutators do not signify a quantum effect.

VIII. USES OF THE PROPOSED CIRCUIT AND ITS GENERALIZATIONS

A. Two-photon detection

A phase qubit with a two-well potential, similar to Fig. 4, can act as a Josephson photomultiplier [34–37]. After such a device absorbs the resonator photon(s), it switches to the true ground state, which indicates the presence of photon(s). One may use two-photon absorption to detect photon pairs.

Consider a device where the excited metastable state tunnels, immediately on absorption, to the deeper well [22,32,33,95]. To achieve fast and incoherent tunneling, the excited state may lie close to the barrier top while the states above and on the other side of the barrier are extremely dissipative. With only two relatively coherent metastable states, our bosonic approximation may break as discussed in Sec. VII. The theory as in Refs. [22,23] may be more appropriate in that case.

Still, we expect that the two-photon coupling rate is $\tilde{g}_2 \approx g_2 \approx 2\pi \times 30$ MHz, approximately as in Fig. 6. This approximate equality is valid even if the small dressing as predicted by the bosonic theory vanishes. As the rate g_2 is below the typical tunneling rates of 50–100 MHz, it limits the detection of a photon pair. Hence, the detection time is about $1/g_2 \approx 10$ ns, comparable to the related device proposed in Ref. [25] with one of the authors.

B. Quantum-nondemolition qubit readout

We can suppress the single-photon coupling $\tilde{g}_-$ while retaining the cross-Kerr one. With purely inductive $g_- = g_1^i$, the bare cross-Kerr K_0 vanishes for the same bias as the bare linear coupling g_-, i.e., at $\delta \mod \pi = \pi/2$. To retain the cross-Kerr interaction while switching off the linear coupling, in Ref. [82] the capacitive coupling shifts the zero of the linear coupling rate, as we illustrate in Fig. 6. In our case, near the zero of $\tilde{g}_-$, the cross-Kerr interaction arises due to asymmetry of the atom potential, even without the capacitive coupling.

As a result, it can be used for qubit readout, similarly to Refs. [96–99]. In Fig. 6, the cross-Kerr coupling rate is about 14 MHz near the point where the linear coupling vanishes. We also need to avoid two-photon exchange. Consider a detuning of $\omega_a - 2\omega_r = 2\pi \times 2$ GHz from the two-photon resonance for the two-photon coupling $g_2 = 2\pi \times 30$ MHz. In that case, the readout is approximately quantum-nondemolition [9,13,100,101], as the cross-Kerr coupling term in the Hamiltonian (12) commutes with the qubit part. In our estimate, we neglect the contribution of $g_2^2/(\omega_a - 2\omega_r) \approx 2\pi \times 1$ MHz to the cross-Kerr rate stemming from the nonresonant two-photon interaction.

Consider using a protocol in Ref. [97] with the resulting cross-Kerr coupling of $K_{0,X} \approx 2\pi \times 16$ MHz. To estimate the readout fidelity $\mathcal{F}$, we assume that the qubit lifetime T_1 is much longer than the measurement time τ_m. Then, according to Refs. [102–104], $\mathcal{F} \approx \frac{1}{2}[1 + e^{-\tau_m/2T_1}\mathrm{erf}(\mathrm{SNR}/\sqrt{8})]$, where erf is the error function. The signal-to-noise ratio (SNR) of the integrated output signal is [13,105,106]

$$\mathrm{SNR} = \sqrt{4\eta\bar{n}_m\tau_m\Gamma_r\frac{K_{0,X}^2}{\Gamma_r^2 + K_{0,X}^2}}. \tag{24}$$

Let us assume there is, on average, $\bar{n}_m = 30$ photons in the probe impulse. To maximize the SNR, we choose the resonator linewidth $\Gamma_r = K_{0,X}$. Consider the quantum efficiency of the readout chain $\eta = 30\%$, which is accessible using near-quantum-limited amplifiers. With the cross-Kerr coupling $K_{0,X}$ as above, the phase qubit in Sec. VI with lifetime $T_1 = 1.6$ μs reported in Ref. [107] can be read out in $\tau_m \approx 30$ ns with over 99.5% fidelity. For a low efficiency $\eta = 5\%$, on par with a setup with no quantum limited-amplifier [98], the fidelity attains its maximum of 97.98% in $\tau_m \approx 105$ ns.

Should the phase qubit as in Sec. VI reach the limit $T_1 \ggg \tau_m$ of long lifetimes, it is read out in $\tau_m \approx 30$ ns with over 99.9% fidelity assuming $\eta = 30\%$. Note that $T_1 \gtrsim 100$ μs has been reported for other superconducting qubits, such as the transmon [108–111] and fluxonium [112–114] qubits.

Besides the phase qubit, the described readout should work for other qubits with an asymmetrical potential. Our theory can also be useful for assessing other [52,82] applications of the cross-Kerr coupling.

IX. CONCLUSIONS

We have calculated dressing of the resonant two-photon and cross-Kerr couplings mediated by a symmetrical SQUID. In a systematic approach, we expand the nonlinear Josephson coupling to the fourth order and account for the leading second-order perturbative corrections. With diagrams, we illustrate some correction processes and elucidate the minimum number of metastable energy states required for our quantitative results to hold.

We argue that the two-photon coupling normally acquires only small corrections, even for higher energies of the Josephson coupling. On the other hand, the cross-Kerr coupling can obtain the most significant renormalization. It arises due to nonlinear coupling and asymmetry in one of the coupled system potentials. For a single-mode resonator coupled to a phase qubit, this correction can reach 15 MHz as

estimated in Sec. VI. While the bare cross-Kerr coupling can be avoided with a proper coupler bias, this dressing part only vanishes with the bias switching off all Josephson-mediated interactions.

We have discussed the validity of our theory in Sec. VII. Most importantly, we have used the bosonic approximation, i.e., we model the artificial atom as an anharmonic oscillator near its metastable minimum. Our quantitative results on the renormalizations depend on that model validity. In Sec. VI, we have provided estimates for an example system. They can be verified with further numerical or experimental studies.

However, we have verified that the virtual processes in the important corrections excite the atom at most to the third excited metastable state. Hence, we expect that our theory should hold reasonably well for a phase qubit with seven coherent metastable states. To count the required number of energy states, we analyze the Schrieffer-Wolff transformations used. This approach may also be used for transmons, whose excitations are bosonic only within a limited number of energy states.

With modifications, the considered circuit can be applied for two-photon detection and qubit readout. If relatively high rates of the cross-Kerr coupling are tolerable or required, our nonlinear coupler may be more favorable than more complex ones, such as a superconducting nonlinear asymmetric inductive element (SNAIL) [68,115], by the fact that it requires fewer junctions. That is especially true when it can be simplified further into a single junction, as discussed in Sec. VI E.

ACKNOWLEDGMENTS

A.M.S. and E.V.S. thank F. Wilhelm-Mauch for discussing our early concepts and results, and R. Baskov for discussions and useful comments. E.V.S. thanks A. Semenov for discussions and useful comments. E.V.S. acknowledges support from the National Research Foundation of Ukraine through the Project No. 2023.03/0165, Quantum correlations of electromagnetic radiation. A.M.S. acknowledges partial support from the Academy of Finland (Contract No. 321982) and the President of Ukraine scholarship for young scientists.

DATA AVAILABILITY

The code that supports the findings of this article is publicly available from Ref. [116].

APPENDIX A: CIRCUIT HAMILTONIAN

In this Appendix, we provide our starting model Hamiltonians for the circuit in Fig. 1. We also write equations to determine the system equilibrium.

1. Fourth-order expansion of Josephson energy

We derived the general circuit Hamiltonian in the preceding work [20], where the resulting expressions are given in Eqs. (1) and (4)–(6). Now we expand it around equilibrium, up to the fourth order in φ_r and φ_a. Then, we arrive at the quantized Hamiltonian

$$\hat{\mathcal{H}} = \hat{\mathcal{H}}_\mathrm{r} + \hat{\mathcal{H}}_\mathrm{a} + \hat{\mathcal{H}}_\mathrm{c} \tag{A1}$$

by imposing the usual commutation relation $[\varphi_\mathrm{r}, n_\mathrm{r}] = i$ for the resonator variables and the analogous one for the rf SQUID. In the Hamiltonian in Eq. (A1), the resonator, atom, and the coupling parts read

$$\hat{\mathcal{H}}_\mathrm{r} \approx 4E_C^\mathrm{r} n_\mathrm{r}^2 + \tfrac{1}{2}\tilde{E}_L^\mathrm{r}\varphi_\mathrm{r}^2 - \tfrac{1}{6}E_\mathrm{J}^\mathrm{c}\varphi_\mathrm{r}^3 \sin\delta - \tfrac{1}{24}E_\mathrm{J}^\mathrm{c}\varphi_\mathrm{r}^4\cos\delta, \tag{A2}$$

$$\hat{\mathcal{H}}_\mathrm{a} \approx 4E_C^\mathrm{a} n_\mathrm{a}^2 + \tfrac{1}{2}\tilde{E}_L^\mathrm{a}\varphi_\mathrm{a}^2 - \tfrac{1}{6}\left(E_\mathrm{J}^\mathrm{a}\sin\phi_\mathrm{a}^\mathrm{min} - E_\mathrm{J}^\mathrm{c}\sin\delta\right)\varphi_\mathrm{a}^3 - \tfrac{1}{24}\left(E_\mathrm{J}^\mathrm{a}\cos\phi_\mathrm{a}^\mathrm{min} + E_\mathrm{J}^\mathrm{c}\cos\delta\right)\varphi_\mathrm{a}^4, \tag{A3}$$

$$\hat{\mathcal{H}}_\mathrm{c} \approx E_C^\mathrm{c} n_\mathrm{a} n_\mathrm{r} - E_\mathrm{J}^\mathrm{c}\varphi_\mathrm{r}\varphi_\mathrm{a}\cos\delta + \tfrac{1}{2}E_\mathrm{J}^\mathrm{c}\left(\varphi_\mathrm{r}^2\varphi_\mathrm{a} - \varphi_\mathrm{r}\varphi_\mathrm{a}^2\right)\sin\delta - \tfrac{1}{4}E_\mathrm{J}^\mathrm{c}\varphi_\mathrm{r}^2\varphi_\mathrm{a}^2\cos\delta + \tfrac{1}{6}E_\mathrm{J}^\mathrm{c}\left(\varphi_\mathrm{r}^3\varphi_\mathrm{a} + \varphi_\mathrm{r}\varphi_\mathrm{a}^3\right)\cos\delta. \tag{A4}$$

Each part consists of the "kinetic" energy contribution quadratic in n_r and n_a, the potential-energy terms quadratic in φ_r and φ_a, and the higher-order terms that give rise to self-nonlinearities and nonlinear interactions.

Compared with the preceding work [20], we rearrange the terms in the Hamiltonians in Eqs. (A2)–(A4). Here the resonator and the atom Hamiltonians accommodate the self-nonlinearities induced by the coupling SQUID.

2. Equilibrium point

Formally, one can find the equations for the equilibrium point from the full dynamical equations. The full Hamiltonian, as provided in the preceding work [20], generates such full equations. Then, setting the derivatives of the phase and charge variables to zero, one obtains

$$E_L^\mathrm{r}\phi_\mathrm{r}^\mathrm{min} + E_\mathrm{J}^\mathrm{c}\sin\delta = 0, \tag{A5a}$$

$$E_L^\mathrm{a}\left(\phi_\mathrm{a}^\mathrm{min} - \frac{2\pi\Phi_\mathrm{e}}{\Phi_0}\right) + E_\mathrm{J}^\mathrm{a}\sin\phi_\mathrm{a}^\mathrm{min} - E_\mathrm{J}^\mathrm{c}\sin\delta = 0, \tag{A5b}$$

where Φ_e is the rf SQUID bias flux and the static phase difference δ is defined in Eq. (2). As discussed in Ref. [20], the equations express the conservation of static currents. Alternatively, Eq. (A5a) can be obtained by finding the screening current induced by the external magnetic field.

3. Hamiltonian with ladder operators

We rewrite the Hamiltonian in Eqs. (A1)–(A4) in terms of the ladder operators introduced in the main text. Hamiltonians of the resonator and artificial atom read

$$\frac{\hat{\mathcal{H}}_\mathrm{r}}{\hbar} = \omega_\mathrm{r}^p\left(a^\dagger a + \frac{1}{2}\right) - X_\mathrm{r}(a^\dagger + a)^3 - Y_\mathrm{r}(a^\dagger + a)^4, \tag{A6}$$

$$\frac{\hat{\mathcal{H}}_\mathrm{a}}{\hbar} = \omega_\mathrm{a}^p\left(b^\dagger b + \frac{1}{2}\right) - X_\mathrm{a}(b^\dagger + b)^3 - Y_\mathrm{a}(b^\dagger + b)^4. \tag{A7}$$

The coupling Hamiltonian in Eq. (A1) becomes

$$\frac{\hat{\mathcal{H}}_\mathrm{c}}{\hbar} = -g_1^c(a^\dagger - a)(b^\dagger - b) - g_1^i(a^\dagger + a)(b^\dagger + b) - \frac{K_0}{4}(a^\dagger + a)^2(b^\dagger + b)^2 - \sum_{n=2,3} g_n(a^\dagger + a)^n(b^\dagger + b) - \sum_{n=2,3} G_n(a^\dagger + a)(b^\dagger + b)^n. \tag{A8}$$

Apart from the bare interactions in Table I, the Hamiltonian describes the three-photon and three–atom-excitation interactions with rates

$$g_3 = -\frac{E_J^c}{6\hbar}\varphi_{r,zpf}^3\varphi_{a,zpf}\cos\delta, \tag{A9}$$

$$G_3 = -\frac{E_J^c}{6\hbar}\varphi_{r,zpf}\varphi_{a,zpf}^3\cos\delta. \tag{A10}$$

They take part in much smaller renormalizations, as derived in Appendix B 2 and discussed in Appendix F.

In addition to the cubic nonlinearity in the atom potential as in Table I in the main text, we provide other self-nonlinearities in the Hamiltonians (A6) and (A7). The quartic term in the atom potential with strength

$$Y_a = \frac{E_J^a\cos\phi_a^{\min} + E_J^c\cos\delta}{24\hbar}\varphi_{a,zpf}^4 \tag{A11}$$

can influence its transition frequency and anharmonicity as estimated in Sec. VI. Similarly to X_a in Eq. (9), one can rewrite it as

$$Y_a = \frac{\eta}{48}\omega_a^p\varphi_{a,zpf}^2, \tag{A12}$$

with $\eta = (\tilde{E}_L^a - E_L^a)/\tilde{E}_L^a \approx \cos\phi_a^{\min}/(\cos\phi_a^{\min} + \beta_L^{-1})$. The resonator self-nonlinearities

$$X_r = \frac{E_J^c}{6\hbar}\varphi_{r,zpf}^3\sin\delta, \quad Y_r = \frac{E_J^c}{24\hbar}\varphi_{r,zpf}^4\cos\delta \tag{A13}$$

arise solely due to the coupling SQUID nonlinearity. They give rise to the resonator anharmonicity, as estimated in Sec. VII B.

APPENDIX B: DERIVATION OF THE RENORMALIZED TWO-PHOTON HAMILTONIAN

In this Appendix, we reduce the approximate circuit Hamiltonian in Appendix A to a variation of the two-photon Jaynes-Cummings model where the artificial atom is modeled as an anharmonic oscillator. First, we show how the nonlinear character of the atom potential gives rise to the cross-Kerr interaction. Then, we calculate renormalizations in the anharmonicities and two-photon coupling, originating from the nonresonant interactions.

1. Eliminating the cubic perturbation

We start by treating the cubic self-nonlinearities in the Hamiltonian from Appendix A 3 as a perturbation. We eliminate them from the Hamiltonian (A7) with a Schrieffer-Wolff transformation [11,69,117,118], $\hat{\mathcal{H}}_a \to e^{-\Lambda_a\mathcal{S}_a}\hat{\mathcal{H}}_a e^{\Lambda_a\mathcal{S}_a}$, where

$$\Lambda_a = \frac{X_a}{\omega_a^p}. \tag{B1}$$

The anti-Hermitian operator $\mathcal{S}_a$ is given by [68,71]

$$\mathcal{S}_a = \tfrac{1}{3}(b^{\dagger 3} - b^3) + 3(b^{\dagger 2}b - b^\dagger b^2) + 3(b^\dagger - b). \tag{B2}$$

For manual calculations, one may rewrite $\mathcal{S}_a$ in terms of $b^\dagger \pm b$ as given in Appendix C. Here, we use the form as in Eq. (B2) and perform the tedious calculations with the computer algebra package QUANTUMALGEBRA.JL [119]. The Jupyter notebook is available from Ref. [116].

Using the Baker-Campbell-Hausdorff (BCH) formula up to the second commutator,

$$e^{-\Lambda_a\mathcal{S}_a}\hat{\mathcal{H}}_a e^{\Lambda_a\mathcal{S}_a} \approx \hat{\mathcal{H}}_a + \Lambda_a[\hat{\mathcal{H}}_a, \mathcal{S}_a] + \frac{\Lambda_a^2}{2}[[\hat{\mathcal{H}}_a, \mathcal{S}_a], \mathcal{S}_a], \tag{B3}$$

we arrive at the Hamiltonian of a quantum anharmonic oscillator,

$$\frac{\hat{\mathcal{H}}_a}{\hbar} \approx \omega_a^p b^\dagger b - \Xi_a b^\dagger b - \frac{\Xi_a}{2}b^{\dagger 2}b^2 + \omega_a^{zpf} + V'_{a3} + V_{a4}, \tag{B4}$$

up to the first order in Λ_a. Here,

$$\Xi_a = 60\Lambda_a X_a + 12Y_a \tag{B5}$$

denotes anharmonicity in the artificial atom energy levels and $\omega_a^{zpf} = \omega_a^p/2 - 11X_a^2/\omega_a^p - 3Y_a$ is its zero-point energy in frequency units. The first term in Eq. (B5) comes from the cubic perturbation in the atom Hamiltonian. With Eq. (B5) for the anharmonicity, Hamiltonian (B4) predicts the same corrections to the energy levels as the textbook calculation in Ref. [120].

On several substitutions, we obtain the atom anharmonicity in terms of the circuit energies,

$$\Xi_a = \frac{E_C^a}{\hbar}\left[\frac{5}{3}\left(\frac{E_L^a}{\tilde{E}_L^a}\right)^2\left(\phi_a^{\min} - \frac{2\pi\Phi_e}{\Phi_0}\right)^2 + \frac{\tilde{E}_L^a - E_L^a}{\tilde{E}_L^a}\right]. \tag{B6}$$

We have used Eqs. (9) and (A11) for X_a and Y_a, the atom plasma frequency in Eqs. (5), its full inductive energy in Eq. (4b), zero-point fluctuations in Eq. (8), and the equation on equilibrium (A5b).

For deriving Eq. (B4), we have assumed that the cubic nonlinearity in the artificial atom is relatively weak with $|\Lambda_a| \ll 1$. Apart from its definition (B1), another way to express this small parameter is

$$\Lambda_a = \frac{\mu}{12}\varphi_{a,zpf}, \tag{B7}$$

where $|\mu| \lesssim 2E_J^a/\tilde{E}_L^a$ is given by Eq. (10) for $E_J^c \lesssim E_J^a$. With that, Eq. (B5) becomes

$$\Xi_a = \tfrac{1}{4}\left(\tfrac{5}{3}\mu^2 + \eta\right)\omega_a^p\varphi_{a,zpf}^2, \tag{B8}$$

where we have also used Eqs. (9) and (A12).

In the atom Hamiltonian (B4), we collect the off-diagonal terms in the last two terms. The penultimate term reads

$$\begin{aligned} V'_{a3} = &-18\Lambda_a X_a(b^{\dagger 2} + b^2) - 12\Lambda_a X_a(b^{\dagger 3}b + b^\dagger b^3) \\ &+ 3\Lambda_a X_a(b^{\dagger 4} + b^4) - 136\Lambda_a Y_a(b^\dagger + b) \\ &- 48\Lambda_a Y_a(b^{\dagger 3} + b^3) - 336\Lambda_a Y_a(b^{\dagger 2}b + b^\dagger b^2) \\ &+ 8\Lambda_a Y_a(b^{\dagger 5} + b^5) - 112\Lambda_a Y_a(b^{\dagger 3}b^2 + b^{\dagger 2}b^3) \\ &- 24\Lambda_a Y_a(b^{\dagger 4}b + b^\dagger b^4) \end{aligned} \tag{B9}$$

and aggregates the terms arising upon transformation of the atom bare Hamiltonian (A7). The last term in Eq. (B4) is the off-diagonal part of the atom quartic self-nonlinearity,

$$V_{a4} = -6Y_a(b^{\dagger 2} + b^2) - 4Y_a(b^{\dagger 3}b + b^\dagger b^3) - Y_a(b^{\dagger 4} + b^4). \tag{B10}$$

Just as for the atom, we apply a Schrieffer-Wolff transformation to the resonator Hamiltonian: $\hat{\mathcal{H}}_\mathrm{r} \to e^{-\Lambda_\mathrm{r}\mathcal{S}_\mathrm{r}}\hat{\mathcal{H}}_\mathrm{r}e^{\Lambda_\mathrm{r}\mathcal{S}_\mathrm{r}}$, where Λ_r reads

$$\Lambda_\mathrm{r} = \frac{X_\mathrm{r}}{\omega_\mathrm{r}^p}. \tag{B11}$$

Note that $|\Lambda_\mathrm{r}| \ll 1$: the resonator cubic nonlinearity is vanishingly small, as its only source is the SQUID coupler. The operator $\mathcal{S}_\mathrm{r}$ is obtained by replacing the atom operators with the resonator ones in Eq. (B2). With the same approximations as in Eq. (B4), we arrive at

$$\frac{\hat{\mathcal{H}}_\mathrm{r}}{\hbar} \approx \omega_\mathrm{r}^p a^\dagger a - \Xi_\mathrm{r} a^\dagger a - \frac{\Xi_\mathrm{r}}{2}a^{\dagger 2}a^2 + \omega_\mathrm{r}^{\mathrm{zpf}} + V'_{\mathrm{r}3} + V_{\mathrm{r}4}, \tag{B12}$$

where $\Xi_\mathrm{r} = 60\Lambda_\mathrm{r}X_\mathrm{r} + 12Y_\mathrm{r}$ is the resonator anharmonicity and $\omega_\mathrm{r}^{\mathrm{zpf}} = \omega_\mathrm{r}^p/2 - 11X_\mathrm{r}^2/\omega_\mathrm{r}^p - 3Y_\mathrm{r}$ is its zero-point energy in the frequency units. We further transform the anharmonicity as

$$\Xi_\mathrm{r} = \frac{E_C^\mathrm{r}}{\hbar}\left[\frac{5}{3}\left(\frac{E_L^\mathrm{r}}{\tilde{E}_L^\mathrm{r}}\phi_\mathrm{r}^{\min}\right)^2 + \frac{\tilde{E}_L^\mathrm{r} - E_L^\mathrm{r}}{\tilde{E}_L^\mathrm{r}}\right], \tag{B13}$$

analogously to Eq. (B6). For a small $E_\mathrm{J}^\mathrm{c}/E_L^\mathrm{r}$, we use $\phi_\mathrm{r}^{\min} \sim E_\mathrm{J}^\mathrm{c}/E_L^\mathrm{r}$ according to Eq. (A5a). That allows us to obtain the leading terms in Eq. (B13),

$$\Xi_\mathrm{r} \approx \frac{E_C^\mathrm{r}}{\hbar}\left[\frac{5}{3}\left(\frac{E_\mathrm{J}^\mathrm{c}}{E_L^\mathrm{r}}\right)^2 \sin^2\delta + \frac{E_\mathrm{J}^\mathrm{c}}{E_L^\mathrm{r}}\cos\delta\right], \tag{B14}$$

where we have also used Eq. (4a).

In the Hamiltonian (B12), $V'_{\mathrm{r}3}$ and $V_{\mathrm{r}4}$ are the off-diagonal terms analogous to those in the atom Hamiltonian (B4). They are obtained by changing the atom notations to the resonator ones in Eqs. (B9) and (B10).

To arrive at the full system Hamiltonian, one also applies the above Schrieffer-Wolff transformations to the coupling part of the circuit Hamiltonian in Appendix A 3. After rearrangement, we write out the full Hamiltonian

$$\begin{aligned}\frac{\hat{\mathcal{H}}}{\hbar} \approx{}& \omega_\mathrm{r}a^\dagger a - \frac{\Xi_\mathrm{r}}{2}a^{\dagger 2}a^2 + V'_{\mathrm{a}3} + V_{\mathrm{a}4} \\ &+ \omega_\mathrm{a}b^\dagger b - \frac{\Xi_\mathrm{a}}{2}b^{\dagger 2}b^2 + V'_{\mathrm{r}3} + V_{\mathrm{r}4} + \frac{\hat{\mathcal{H}}_\mathrm{I}}{\hbar}\end{aligned} \tag{B15}$$

up to the zero-point energy. Here, $\omega_\mathrm{r} = \omega_\mathrm{r}^p - \Xi_\mathrm{r} - K_{0,X}/2$ and $\omega_\mathrm{a} = \omega_\mathrm{a}^p - \Xi_\mathrm{a} - K_{0,X}/2$ denote the resonator and the atom frequencies with

$$K_{0,X} \approx K_0 + 24\Lambda_\mathrm{a}g_2 + 24\Lambda_\mathrm{r}G_2. \tag{B16}$$

We obtain Eq. (14) in Sec. V A by using Eq. (B1) and neglecting the last term in the above expression. That is always possible when the resonator cubic nonlinearity is much weaker than in the atom, i.e., when $|\Lambda_\mathrm{r}| \ll |\Lambda_\mathrm{a}|$; and when, at the same time, $|g_2| \sim |G_2|$. The latter is true when the vacuum fluctuations in the resonator and the artificial atom $\varphi_{\mathrm{r,zpf}} \sim \varphi_{\mathrm{a,zpf}}$ are comparable. A more general criterion for the approximation in Eq. (14) to hold, $(E_L^\mathrm{a}/E_\mathrm{J}^\mathrm{a} + \cot\phi_\mathrm{a}^{\min})\sin\delta \lesssim 1$, is obtained by taking into account the condition (13) of no ultrastrong coupling. Using the definition of Λ_a in Eq. (B1) along with the expressions for X_a and g_2 from Table I in the above expression for $K_{0,X}$, one obtains Eq. (15) in Sec. V A.

In Eq. (B15), the Hamiltonian $\hat{\mathcal{H}}_\mathrm{I}$ aggregates all interaction terms; as it is cumbersome, we do not present its full form. However, by proper adjustment of the resonator and the atom frequencies, one can make their two-photon coupling dominant. Most other couplings then act as perturbations and renormalize the resonant interactions. We treat them in what follows.

2. Two-photon regime

With $\omega_\mathrm{a} \approx 2\omega_\mathrm{r}$, close to the two-photon resonance, the interaction Hamiltonian becomes

$$\frac{\hat{\mathcal{H}}_\mathrm{I}}{\hbar} = -g_2(a^{\dagger 2}b + b^\dagger a^2) - K_{0,X}a^\dagger a\, b^\dagger b + \frac{\delta\hat{\mathcal{H}}_\mathrm{I}}{\hbar}. \tag{B17}$$

The first two terms here correspond to the resonant interactions: the bare two-photon coupling of strength g_2 and the cross-Kerr coupling of strength $K_{0,X}$ as given by Eq. (B16). Below, we calculate the essential renormalizations to these couplings.

We collect the nonresonant terms that produce nonnegligible renormalizations into

$$\begin{aligned}\frac{\delta\hat{\mathcal{H}}_\mathrm{I}}{\hbar} \approx{}& \tilde{g}_-(a^\dagger b + b^\dagger a) - \tilde{g}_+(a^\dagger b^\dagger + ba) \\ &- 3g_3(b^\dagger a^\dagger a^2 + a^{\dagger 2}ab) - 3g_3(b^\dagger a^{\dagger 2}a + a^\dagger a^2 b) \\ &- F(a^\dagger b^\dagger b^2 + b^{\dagger 2}ba) - F(a^\dagger b^{\dagger 2}b + b^\dagger b^2 a) \\ &- g_2(2a^\dagger a + 1)(b^\dagger + b) - J(2b^\dagger b + 1)(a^\dagger + a) \\ &- g_2(a^{\dagger 2}b^\dagger + a^2 b) - \tilde{G}_2^-(a^\dagger b^2 + b^{\dagger 2}a) \\ &- \tilde{G}_2^+(a^\dagger b^{\dagger 2} + b^2 a).\end{aligned} \tag{B18}$$

We treat $\delta\hat{\mathcal{H}}_\mathrm{I}$ as a perturbation in Appendix B 2 c. We discuss the terms neglected in $\delta\hat{\mathcal{H}}_\mathrm{I}$ in Appendixes B 2 a and B 2 b.

The first two terms in the perturbation Hamiltonian (B18) correspond to the number-conserving and number-nonconserving parts of the linear interaction as described in Table I. Their coupling rates $\tilde{g}_\pm = g_1^c \pm \tilde{g}_1^i$ include contributions from both capacitive and inductive couplings. The latter coupling strength renormalizes as

$$\tilde{g}_1^i \approx g_1^i + 20\Lambda_\mathrm{a}G_2, \tag{B19}$$

where we neglect a contribution of $3(g_3 + G_3)$ from the fourth-order expansion term in the coupler Josephson energy. Indeed, when $E_C^\mathrm{r} \lll \tilde{E}_L^\mathrm{r}$ and $E_C^\mathrm{a} \lll \tilde{E}_L^\mathrm{a}$, the relevant vacuum fluctuations are small with $\varphi_{\mathrm{r,zpf}}^2, \varphi_{\mathrm{a,zpf}}^2 \ll 1$. Thus, $3|g_3 + G_3| \ll |g_1^i|$ as follows from the definition of g_1^i in Table I and g_3 with G_3 in Appendix A 3. As for the second term in Eq. (B19), it matters near the points $\delta \mod \pi = \pi/2$ where the bare inductive coupling g_1^i vanishes.

Away from there, the entire renormalization of the linear coupling g_1^i often can be negligible. The coupling strength G_2 is of higher order in the vacuum fluctuations compared with g_1^i. Thus, we have that $20\Lambda_\mathrm{a}|G_2| \ll |g_1^i|$ as far as $\mu\varphi_{\mathrm{a,zpf}}^2|\tan\delta| \ll 1$. In that case, $\tilde{g}_1^i \approx g_1^i$ according to Eq. (B19).

The second and third lines in Eq. (B18) describe nonlinear interactions that result in the same transitions as the linear coupling. The number-conserving part of such interactions

is known as a nonlinear Jaynes-Cummings interaction (see Ref. [121] and the references therein). Unlike the regular linear interactions, excitation and deexcitation of the atom occur in two steps here. Consider the second line in Eq. (B18) describing couplings of rate $3g_3$, whose energies are cubic in the resonator variables. Here, during the excitation, the resonator first goes two energy levels up and then one level down. Up to the order of creation and annihilation processes, this interaction is a linear coupling with its strength modulated by the photon number $a^\dagger a$. The third line in Eq. (B18) contains analogous terms with the roles of the atom and resonator reversed. However, the rate of these couplings renormalizes as

$$F = 3G_3 + 20\Lambda_a G_2, \tag{B20}$$

similarly to the linear inductive coupling in Eq. (B19) and as described in Sec. V B of the main text.

The fourth line in Eq. (B18) describes the couplings of optomechanical type. One of them has its strength renormalized as

$$J = G_2 + 6\Lambda_a g_1^i. \tag{B21}$$

Plugging g_1^i and G_2 from Table I along with Eqs. (B1) and (B7) for Λ_a yields the expression in Appendix F 1.

The penultimate line in Eq. (B18) describes the energy-nonconserving two-photon coupling. With rate g_2, it simultaneously excites or deexcites the resonator by one energy level and the atom by two energy levels. The last line in Eq. (B18) describes two–atom-excitation interactions illustrated in Table I. They are dressed as

$$\tilde{G}_2^{\pm} = G_2 - 2\Lambda_a\left(g_1^i \pm 2g_1^c\right). \tag{B22}$$

The second term arises from the capacitive and inductive couplings as the atom dresses by its cubic nonlinearity.

a. Further approximations in treating self-nonlinearities

In Appendix B 1, we restrict the perturbation theory to second order in the cubic perturbation. We need further simplifications to arrive at the Hamiltonian in Eqs. (B17) and (B18).

First, consider the off-diagonal noncoupling terms in Eqs. (B9) and (B10). Recall that V'_{a3} arises upon transforming the atom bare Hamiltonian in Eq. (A7), while V_{a4} is the off-diagonal part of its quartic nonlinearity. The coefficients in V'_{a3} and V_{a4} are roughly as the atom anharmonicity Ξ_a in the magnitude. In the second-order perturbation theory, this brings different energy terms of about $\hbar\Xi_a^2/\omega_a$. They are small for small anharmonicity

$$\Xi_a \ll \omega_a. \tag{B23}$$

We provide specific criteria to neglect such terms in the frequencies, as well as in the single-photon and two-photon coupling rates. Note that V'_{r3} and V_{r4} give rise to even smaller contributions as the induced resonator anharmonicity is small with $|\Xi_r| \ll |\Xi_a|$.

Similarly to the cubic terms in Appendix B 1, one can approximately eliminate V'_{a3} and V_{a4} with a Schrieffer-Wolff transformation $\exp(\mathcal{S}'_a)$ with

$$\begin{aligned}\mathcal{S}'_a = \Bigg(&\frac{3\Lambda_a X_a - Y_a}{4\omega_a} b^{\dagger 4} + \frac{12\Lambda_a X_a + 4Y_a}{2\omega_a} b^{\dagger 3} b \\ &+ \frac{18\Lambda_a X_a + 6Y_a}{2\omega_a} b^{\dagger 2} + \frac{8\Lambda_a Y_a}{5\omega_a} b^{\dagger 5} - \frac{24\Lambda_a Y_a}{3\omega_a} b^{\dagger 4} b \\ &- \frac{112\Lambda_a Y_a}{\omega_a} b^{\dagger 3} b^2 - \frac{48\Lambda_a Y_a}{3\omega_a} b^{\dagger 3} - \frac{336\Lambda_a Y_a}{\omega_a} b^{\dagger 2} b \\ &- \frac{136\Lambda_a Y_a}{\omega_a} b^\dagger\Bigg) - \text{H.c.}\end{aligned}$$

Applying it to the Hamiltonian (B4) renormalizes the atom frequency by about $-(\omega_a/12)(\mu^2+\eta)^2\varphi_{a,zpf}^4$. Under normal conditions, this dressing is smaller than the two-photon coupling strength and hence does not affect the resonance. Roughly, that is the case for $|g_2| > \Xi_a^2/\omega_a$. Note that, upon transformation, the atom anharmonicity also acquires a dressing; it is small when Eq. (B23) holds.

Elimination of the off-diagonal terms in Eq. (B4) dresses the interactions in Eq. (B18) as well. Particularly, that adds $(\mu^2+\eta)\varphi_{a,zpf}^2 g_1^i/8$ into the inductive coupling rate g_i. However, this correction is smaller than $3(g_3+G_3)$ neglected in Eq. (B19) since $(\mu^2+\eta)/8 < 1$ for $\mu \lesssim 2$. The two-photon coupling also gets dressed by the terms in Eq. (B9). It acquires a correction of $(\mu^2+\eta)\varphi_{a,zpf}^2 g_2/8$. However, it is of the fifth order in the zero-point fluctuations and of the first order in the coupler energy E_J^c. Hence it exceeds the accuracy of our approximation in the Hamiltonian (A8) regardless of E_J^c magnitude. From the other point of view, one mentions that both corrections are small with a relatively small atom anharmonicity as in Eq. (B23).

b. Approximations in coupling dressed by the cubic perturbation

In Hamiltonian (B17), we group the "new" perturbations into $\delta\hat{\mathcal{H}}_I$ in Eq. (B18). There, we retain only the terms that provide essential renormalizations. Dressing the coupling terms in the bare Hamiltonian (A8) of Appendix A 3 not only renormalizes them but also creates new couplings different from those in the bare interaction Hamiltonian (A8). However, they are of magnitudes comparable to the same-type terms that we neglect in the cosine expansion [20] of the coupler energy in Eq. (A8). In other words, they are of the same order in the zero-point fluctuations $\varphi_{r,zpf}$ and $\varphi_{a,zpf}$ and the Josephson energy of the coupler E_J^c. Therefore, we omit these new couplings in Eq. (B18) as they exceed the accuracy of our approximation in the Hamiltonian (A8).

In addition to the negligible new couplings, small coupling terms of the same type as in the Hamiltonian (A8) also arise in Eq. (B17). They read

$$\begin{aligned}\frac{\delta\hat{h}_I}{\hbar} = &-\tilde{G}_3(a^\dagger + a)(b^{\dagger 3} + b^3) \\ &- g_3(a^{\dagger 3} + a^3)(b^\dagger + b) \\ &- \frac{\tilde{K}_0}{4}(a^\dagger + a)^2(b^{\dagger 2} + b^2) \\ &- \frac{K_{0,X}}{4}(2b^\dagger b + 1)(a^{\dagger 2} + a^2),\end{aligned} \tag{B24}$$

with $\tilde{G}_3 = G_3 - 4\Lambda_a G_2$ and $\tilde{K}_0 = K_0 - 8\Lambda_a g_2$. These terms yield only negligible corrections to the frequencies and to the cross-Kerr and two-photon interaction rates. We have verified that such corrections appear at least in the seventh order in the zero-point fluctuations $\varphi_{r,zpf}$ and $\varphi_{a,zpf}$. Hence they are beyond the accuracy of our expressions.

In Eqs. (B18) and (B24), we account for the corrections proportional to Λ_a in the coupling rates. At the same time, we neglect the other corrections with Λ_r, since $|\Lambda_r| \ll |\Lambda_a|$.

c. Elimination of nonresonant linear and optomechanical interactions

Here we calculate corrections in the two-photon coupling and the effective resonator anharmonicity.

The perturbation $\delta\hat{\mathcal{H}}_I$ can be approximately eliminated via the Schrieffer-Wolff transformation $\hat{\mathcal{H}} \to e^{-\mathcal{W}}\hat{\mathcal{H}}e^{\mathcal{W}}$, where the anti-Hermitian operator $\mathcal{W}$ reads

$$\begin{aligned}\mathcal{W} =& \lambda_-(a^\dagger b - b^\dagger a) + \lambda_+(a^\dagger b^\dagger - ba)\\ &+ \zeta_-(b^{\dagger 2}ba - a^\dagger b^\dagger b^2) + \zeta_+(a^\dagger b^{\dagger 2}b - b^\dagger b^2 a)\\ &+ \vartheta_-(b^\dagger a^\dagger a^2 - a^{\dagger 2}ab) + \vartheta_+(b^\dagger a^{\dagger 2}a - a^\dagger a^2 b)\\ &+ \lambda_r\left(a^\dagger a + \tfrac{1}{2}\right)(b - b^\dagger) + \lambda_a\left(b^\dagger b + \tfrac{1}{2}\right)(a - a^\dagger)\\ &+ \lambda_2(a^{\dagger 2}b^\dagger - ba^2) + \eta_+(a^\dagger b^{\dagger 2} - b^2 a)\\ &+ \eta_-(b^{\dagger 2}a - a^\dagger b^2). \end{aligned} \tag{B25}$$

The small parameters $\lambda_\pm,\ \lambda_r,\ \lambda_a,\ \lambda_2,\ \zeta_\pm,\ \vartheta_\pm,\ \eta_\pm \ll 1$ read

$$\begin{aligned}&\lambda_\pm = \frac{\tilde{g}_\pm}{\omega_a \pm \omega_r}, \quad \zeta_\pm = \frac{F}{\omega_a \pm \omega_r - \Xi_a}, \quad \vartheta_\pm = \frac{3g_3}{\omega_a \pm \omega_r},\\ &\lambda_r = -\frac{2g_2}{\omega_a}, \quad \lambda_a = -\frac{2J}{\omega_r}, \quad \lambda_2 = \frac{g_2}{\omega_a + 2\omega_r},\\ &\eta_\pm = \frac{\tilde{G}_2^\pm}{2\omega_a \pm \omega_r - \Xi_a}. \end{aligned} \tag{B26}$$

Now we use the approximate BCH formula as for Eqs. (B4) and (B12). With the operator $\mathcal{W}$ and the Hamiltonian in Eqs. (B15), (B17), and (B18), we obtain

$$\begin{aligned}\frac{\hat{\mathcal{H}}}{\hbar} \approx& \omega_r a^\dagger a - \frac{\Xi_r'}{2}a^{\dagger 2}a^2 + \omega_a b^\dagger b - \frac{\Xi_a'}{2}b^{\dagger 2}b^2\\ &- K_{0,X}a^\dagger a b^\dagger b - \tilde{g}_2(a^{\dagger 2}b + b^\dagger a^2). \end{aligned} \tag{B27}$$

Here, we have omitted the higher-order nonlinearities exceeding the accuracy of the approximation in Eqs. (A6) and (A7).

In this contribution, we omit further dressing of the transition frequencies ω_r and ω_a. They are of the second order in the small parameters in Eqs. (B26). We assume that the two-photon coupling rate is much larger than these corrections and hence they do not influence the resonance condition. We also omit the anharmonicity dressing, as well as the further dressing in the cross-Kerr coupling as discussed in Sec. V A. Note that calculation of the cross-Kerr dressing by other interactions requires taking into account V_{a3}' and V_{a4} in Eqs. (B9) and (B10). We leave derivation and analysis of these corrections for future work.

Here we only calculate the renormalized two-photon coupling strength,

$$\begin{aligned}\tilde{g}_2 =& g_2 + \frac{\lambda_a}{2}g_- - \lambda_- J\\ &+ \eta_- g_+ + \lambda_+ \tilde{G}_2^- + 2\lambda_+\eta_-\Xi_a. \end{aligned} \tag{B28}$$

We have dropped the corrections $\zeta_+\tilde{G}_2^- + \eta_- F + \frac{3}{2}(\vartheta_- J - \frac{3}{2}\lambda_a g_3) + 2\eta_-\zeta_+\Xi_a$ as they are of the seventh order in the zero-point fluctuations $\varphi_{r,zpf}$ and $\varphi_{a,zpf}$ and hence beyond the accuracy of the Hamiltonian in Eq. (A8). We leave the terms of the fifth order in $\varphi_{r,zpf}$ and $\varphi_{a,zpf}$. They can be relevant as explained in Sec. V C.

APPENDIX C: CALCULATION OF THE MAIN CROSS-KERR CORRECTION WITH WICK'S THEOREM

On the transformations in Appendix B, the interactions we are interested in pick up corrections. Each transformation is designed to compensate for the direct action of a nonresonant coupling in the resulting frame. A nonlinear nonresonant coupling requires a polynomial of the same order in the transformation exponent. When a transformation is complicated, such as in Eq. (B2), it becomes nontrivial to trace the origin of the interaction renormalizations.

That is especially concerning for a phase qubit as in Sec. VI. Its metastable well holds a finite number of energy states; hence a virtual process climbing too high does not occur as predicted by our anharmonic oscillator model. It is then of interest to determine how far up the processes in each correction do climb.

In this Appendix, we demonstrate how to use Wick's theorem [122,123] to calculate the coupling corrections. That provides some grounding for laying out the virtual processes in the diagrams in Figs. 2 and 3. For the phase qubit as in Sec. VI, the most vivid correction due to the virtual processes appears in the cross-Kerr coupling strength. We, therefore, focus on the cross-Kerr correction here.

1. Calculation

Beforehand, it is convenient to rewrite Eq. (B2) that we use in Appendix B as

$$\mathcal{S}_a = -\tfrac{2}{3}(b^\dagger - b)^3 + (b^\dagger + b)^2(b^\dagger - b) - 2(b^\dagger + b). \tag{C1}$$

We verify [116] this form with PYBOLANO [124], which is based on Refs. [125,126]. With Eq. (C1), the commutators in the BCH formula (B3) are easy to calculate, as our bare coupling Hamiltonian (A8) in Appendix A 3 depends on the dimensionless canonical coordinates $b^\dagger + b$ and $i(b^\dagger - b)$. Note that Refs. [127,128] provide their starting Hamiltonians in such form.

Below, we show that dressing of the coupling energy

$$I_{20} = \hbar g_2 (a + a^\dagger)^2 (b + b^\dagger) \tag{C2}$$

quadratic in the resonator operators [see Eq. (A8)] gives rise to the cross-Kerr coupling. More precisely, the cross-Kerr correction in Eqs. (14) and (15) arises from expanding the transformation exponent to the first order in Λ_a,

$$I_{20} \to e^{-\Lambda_a \mathcal{S}_a} I_{20} e^{\Lambda_a \mathcal{S}_a} \approx I_{20} + \Lambda_a (I_{20}\mathcal{S}_a - \mathcal{S}_a I_{20}). \tag{C3}$$

Here $\Lambda_a = X_a/\omega_a^p$, as defined in Eq. (B1).

While it is trivial to calculate our commutator in Eq. (C3), the calculation can become more involved for higher nonlinearities. We use Wick's theorem because it makes the manual treatment tractable for more complex cases. Additionally, it yields the result in normal order.

Thus, we use it to calculate the correction, i.e., the last term on the right-hand side of Eq. (C3). We denote

$$P = b^\dagger + b, \quad M = b^\dagger - b. \tag{C4}$$

Then, noting that only single contractions bring the terms with $b^\dagger b$, we write them out for

$$(b^\dagger + b)\mathcal{S} = -\frac{2\times 3}{3} : \overbrace{PMMM} : -\frac{2}{3}C_3^2 : P\overbrace{MMM} : + 3 : PP\,\overline{PM}: -C_3^2 : \overline{PP}\,PM : + \cdots \tag{C5}$$

and

$$\mathcal{S}(b^\dagger + b) = 2 : P\,\overline{PM}\,P : - : P\,\overline{PM}\,P : + \cdots, \tag{C6}$$

where $C_n^k = n!/[k!(n-k)!]$ denotes a binomial coefficient, $: O :$ denotes the operation of normal ordering applied to an operator O, and contraction is defined as $\overline{AB} = AB - : AB :$.

In Eq. (C5), the first two terms are the contractions with the first term $-2M^3/3$ in Eq. (C1). The other two are the contractions with the second term P^2M there. In Eq. (C6), both terms are due to the second term P^2M in Eq. (C1). Each contraction coefficient includes a factor that counts the contractions alike, such as $:\overline{PM}\,MM:$, $:\overbrace{PMMM}:$, and $:\overbrace{PMMM}:$ for the first term in Eq. (C5).

We note that $\overline{PP} = 1$, $\overline{MM} = -1$, and $\overline{PM} = 1$. Then using Eqs. (C5) and (C6), one can check that the cross-Kerr term proportional to $a^\dagger a\, b^\dagger b$ comes with a coefficient of $24 g_2 \Lambda_a$ in Eq. (C3). That is the same coefficient as in Eqs. (14) and (B16) according to the calculation of the correction in Appendix B.

2. Diagrams and the number of energy levels

The atom part of the diagram in Fig. 2(a) shows the process as described, among others, by the term $: P\,\overline{MM}\,M :$ similar to the second term in Eq. (C5). A contraction in a term corresponds to a loop in the diagram. Note that, when only taking into account the first BCH commutator as in Eq. (C3), the processes from different interactions do not mix.

The normal-ordered products as in Eqs. (C5) and (C6) directly provide the cross-Kerr coupling Hamiltonian in a convenient form. Wick's theorem automatically takes into account that the $bb^\dagger$ products in Eq. (C3) yield the normally ordered $b^\dagger b$. The associated use of commutation relations—bosonic in our case—is exact within the model; however, with it we lose the information on how far up in the energy ladder a process goes.

Based on the structure of the normally ordered terms in Eqs. (C5) and (C6), we can recover that from Eq. (C3). In the case of the cross-Kerr correction, we simply notice that some of the $b^\dagger b$ processes actually arise from the $bb^\dagger$ ones that bring the atom higher in its energy levels. One such sequence is depicted in Fig. 2(a) with dashed lines.

Note that, for determining the number of energy states required, one can consider normally ordered I_{20} and $\mathcal{S}_a$ in Eq. (C3). In this form, each describes processes that excite the atom as little as possible while still providing the required results. For example, consider the case when the next higher-energy state decays faster than the interaction can occur, due to reasons *beyond* our simple anharmonic oscillator model. In that case, the coupling energy I_{20} cast in the normally ordered form clearly describes the interactions in the same way. The same applies to $\mathcal{S}_a$, which is responsible in Eq. (C3) for an approximate unitary transformation.

That is not the case for further normal ordering in the equation. In Eq. (C3), $bb^\dagger$ and $b^\dagger b + 1$ can differ as the bosonic approximation breaks. If the excitations in $\mathcal{S}_a$ or I_{20} bring the atom into, e.g., a rapidly decaying state, the respective processes yield different states. Our approximate unitary transformation does not work as intended, as the corresponding (virtual) processes occur differently. However, these very processes are supposed to yield the interactions in the transformed picture. Therefore, if we further normal-order Eq. (C3), this can hide such an issue and may predict interaction terms in the Hamiltonian with remarkably incorrect amplitudes or even structure.

APPENDIX D: HIGHEST-CLIMBING PROCESSES

In Figs. 2 and 3, the correction processes climb the atom energy ladder as high as possible. We provide a recipe to determine such processes:

(1) Determine a Schrieffer-Wolff transformation to take into account nonresonant interactions perturbatively. For several transformations, the recipe applies recursively. For example, see Fig. 3(b) explained in Appendix F 2.

(2) Take one operator sequence from an interaction term in the Hamiltonian and another one from the transformation exponent. It is convenient to assign a color to each sequence. The available operators should accomplish the required interaction. One can vary the order of sequences but cannot intermix operators of different colors. One may contract pairs of creation and annihilation operators into unity.

(3) Show a loop heading upward when contracting $bb^\dagger$ and a loop downward when contracting $b^\dagger b$.

(4) Only two-color loops require the next energy level to be available. Hence, no energy levels on top of the single-color loops in Figs. 2 and 3.

(5) Consider a sequence that increases the energy more than the other ones, possibly between other sequences. Then place it next to the highest of the two energy levels at the ends of the interaction to be realized.

Let us comment on some of the rules. Consider rule 2. The sequence order can be changed, as formally the whole of each correction stems from a commutator (see Appendix C), where the sequences occur in both orders. Contractions in rules 2 and 3 are discussed in Appendix C and in the caption of Fig. 2. For the motivation of rule (4), refer to Appendix C.

APPENDIX E: CALCULATION OF THE MAIN CROSS-KERR CORRECTION USING DYNAMICAL EQUATIONS

Consider for simplicity the Hamiltonian $H/\hbar = \omega_r a^\dagger a + \omega_a b^\dagger b - g_2(a^\dagger + a)^2(b^\dagger + b) - X_a(b^\dagger + b)^3$. It contains the necessary terms to obtain the cross-Kerr correction due to the

potential asymmetry and nonlinear coupling. Here we obtain this cross-Kerr rate by analyzing the dynamical equations and their formal solutions, following from the Hamiltonian.

The Heisenberg equation of motion for the atom lowering operator is obtained as $\dot{b} = \frac{1}{i\hbar}[b, H]$ and reads

$$\dot{b} = -i\omega_a b + 3iX_a(b^\dagger + b)^2 + ig_2(a^\dagger + a)^2. \tag{E1}$$

A formal solution of this equation is

$$b(t) = b(0)e^{-i\omega_a t} + 3iX_a \int_0^t dt' e^{-i\omega_a(t-t')}(b^\dagger + b)_{t'}^2 + ig_2 \int_0^t dt' e^{-i\omega_a(t-t')}(a^\dagger + a)_{t'}^2. \tag{E2}$$

We assume that $a^\dagger a$ changes slowly on the timescales of the observation time t. Integrating the last term yields $(g_2/\omega_a)(2a^\dagger a + 1)$ and some oscillating terms. We plug that back into the dynamical Eq. (E1) to obtain

$$\dot{b} \approx -i\left(\omega_a - \frac{12g_2X_a}{\omega_a}\right)b + \frac{24ig_2X_a}{\omega_a}ba^\dagger a + ig_2(a^\dagger + a)^2 + \text{anharmonicity terms}. \tag{E3}$$

Here we neglect the nonresonant contribution in the second term on the right-hand side. The resulting term is approximately as obtained from the Hamiltonian with the cross-Kerr correction in Eq. (14) from Sec. V A.

The atom frequency in Eq. (E3) coincides with Eqs. (20) and (14) with $K_0 = 0$. Existence of the population-independent frequency shift $12g_2X_a/\omega_a$ relies on commuting a and $a^\dagger$ in Eq. (E2). Hence, unlike the cross-Kerr term, it vanishes in the classical limit.

APPENDIX F: OTHER INTERACTION DRESSING

In this Appendix, we explain other small renormalizations in the resonant two-photon and in the nonresonant optomechanical-like couplings. We often call the coupling types by their bare rates here. For details, refer to Table I in the main text and the bare coupling Hamiltonian (A8) in Appendix A 3.

1. Nonresonant optomechanical interactions

As pointed out in Table I, the coupling term with G_2 yields a reverse optomechanical-like interaction. Owing to a combination of inductive interactions with the atom cubic nonlinearity, this optomechanical coupling renormalizes as $G_2 \to J$, with the full coupling rate

$$J = G_2 + \frac{6g_1^iX_a}{\omega_a^p} \tag{F1}$$

$$\approx \frac{E_J^c}{2\hbar}(\sin\delta - \mu\cos\delta)\,\varphi_{r,zpf}\varphi_{a,zpf}^2. \tag{F2}$$

This correction to the G_2 interaction can be interpreted similarly to Eq. (16) of the main text.

Within our assumptions, the optomechanical g_2 interaction retains its bare magnitude as in Table I. This asymmetry, as seen from Table I and Eq. (F2), is due to the cubic nonlinearity in the potential of the atom that is negligible in the resonator.

2. Details of two-photon corrections

Here we provide and interpret expressions for the two-photon corrections for reasonably strong Josephson coupling. Assuming a relatively small atom anharmonicity, $|\Xi_a| \ll \omega_a$, we obtain from the results of Appendix B 2 that

$$\tilde{g}_2 \approx g_2 - \frac{2g_-J}{\omega_r} + \frac{2g_+G_2}{3\omega_r} - \frac{\mu g_+(g_1^i - 2g_1^c)\varphi_{a,zpf}}{9\omega_r} \tag{F3}$$

for the two-photon coupling rate in the Hamiltonian (12). The last three terms are due to various perturbative corrections. As pointed out in Sec. V C, they are nonnegligible for higher coupling energies as in Eq. (18). We discuss these corrections below.

Consider the correction in the second term in Eq. (F3). This correction is due to chaining of the single-photon and optomechanical virtual processes. We depict one such sequence with a bare optomechanical process in Fig. 3(a). Another one arises through its dressed part in Eq. (F1). In other words, linear inductive interaction chains with the full number-conserving one and the atom cubic nonlinearity. We depict one such sequence with a number-nonconserving part of the inductive interaction in Fig. 3(b).

The correction as in the third term in Eq. (F3) can be depicted similarly to the second term; see Fig. 3(c). Here, however, a G_2 interaction that doubly (de)excites the atom chains with the number-nonconserving linear interaction. As before, in Fig. 3(c) we choose the particular processes so that the other similar ones do not excite the atom higher.

Now consider the two-photon correction in the last term in Eq. (F3). It arises, among others, owing to a process similar to that in Fig. 3(b) and uses four energy states of the atom. This term is considerably smaller than the other corrections, owing to the coefficient of $\mu/9$. Still, the term can be significant with even smaller zero-point fluctuations or when the capacitive coupling is much stronger than the inductive one with $g_1^c \gg g_1^i$.

The latter case is unlikely when one aims at stronger two-photon coupling. We expect g_1^c to be of the same order or smaller than the maximal value of the inductive coupling rate $(g_1^i)_{max}$. Both couplings are limited by the criterion $g_- = g_1^c - g_1^i \ll \omega_r, \omega_a$, disallowing ultrastrong coupling. Practically, one raises the coupler Josephson energy E_J^c to reach higher two-photon coupling strength $g_2 \propto E_J^c/\hbar$; that raises $g_1^i \propto E_J^c/\hbar$ proportionally. Therefore, for such an application, it is unlikely that $g_1^c \gg (g_1^i)_{max}$, as that severely limits the magnitudes of $(g_1^i)_{max}$ and hence g_2.

In the derivation of Eq. (F3) in Appendix B 2, we neglect perturbative corrections of seventh order in the zero-point fluctuations $\varphi_{a,zpf}$ and $\varphi_{r,zpf}$. In principle, they can exceed the fifth-order terms in the expansion of the Josephson coupling energy. However, that occurs with even higher coupling energies E_J^c as in $\varphi_{zpf}^2 E_J^c \gtrsim \hbar\omega_r$ assuming $\varphi_{zpf} \sim \varphi_{a,zpf} \sim \varphi_{r,zpf}$. For similar reasons, in Eq. (F3), we use the bare value of the linear coupling rates $g_\pm$ as in Table I.

[1] E. T. Jaynes and F. W. Cummings, Comparison of quantum and semiclassical radiation theories with application to the beam maser, Proc. IEEE **51**, 89 (1963).

[2] F. Yan, P. Krantz, Y. Sung, M. Kjaergaard, D. L. Campbell, T. P. Orlando, S. Gustavsson, and W. D. Oliver, Tunable coupling scheme for implementing high-fidelity two-qubit gates, Phys. Rev. Appl. **10**, 054062 (2018).

[3] E. A. Sete, A. Q. Chen, R. Manenti, S. Kulshreshtha, and S. Poletto, Floating tunable coupler for scalable quantum computing architectures, Phys. Rev. Appl. **15**, 064063 (2021).

[4] F. Marxer, A. Vepsäläinen, S. W. Jolin, J. Tuorila, A. Landra, C. Ockeloen-Korppi, W. Liu, O. Ahonen, A. Auer, L. Belzane, V. Bergholm, C. F. Chan, K. W. Chan, T. Hiltunen, J. Hotari, E. Hyyppä, J. Ikonen, D. Janzso, M. Koistinen, J. Kotilahti, *et al.*, Long-distance transmon coupler with CZ-gate fidelity above 99.8%, PRX Quantum **4**, 010314 (2023).

[5] L. Abdurakhimov, J. Adam, H. Ahmad, O. Ahonen, M. Algaba, G. Alonso, V. Bergholm, R. Beriwal, M. Beuerle, C. Bockstiegel, *et al.*, Technology and performance benchmarks of IQM's 20-qubit quantum computer, arXiv:2408.12433.

[6] J. Koch, T. M. Yu, J. Gambetta, A. A. Houck, D. I. Schuster, J. Majer, A. Blais, M. H. Devoret, S. M. Girvin, and R. J. Schoelkopf, Charge-insensitive qubit design derived from the Cooper pair box, Phys. Rev. A **76**, 042319 (2007).

[7] F. Solgun and S. Srinivasan, Direct calculation of *ZZ* interaction rates in multimode circuit quantum electrodynamics, Phys. Rev. Appl. **18**, 044025 (2022).

[8] R. W. Boyd, *Nonlinear Optics*, 4th ed. (Academic Press, London, 2008).

[9] S. Haroche, Cavity quantum electrodynamics: A review of Rydberg atom-microwave experiments on entanglement and decoherence, AIP Conf. Proc. **464**, 45 (1999).

[10] P. Carbonaro, G. Compagno, and F. Persico, Canonical dressing of atoms by intense radiation fields, Phys. Lett. A **73**, 97 (1979).

[11] A. Blais, R.-S. Huang, A. Wallraff, S. M. Girvin, and R. J. Schoelkopf, Cavity quantum electrodynamics for superconducting electrical circuits: An architecture for quantum computation, Phys. Rev. A **69**, 062320 (2004).

[12] A. Blais, J. Gambetta, A. Wallraff, D. I. Schuster, S. M. Girvin, M. H. Devoret, and R. J. Schoelkopf, Quantum-information processing with circuit quantum electrodynamics, Phys. Rev. A **75**, 032329 (2007).

[13] A. Blais, A. L. Grimsmo, S. M. Girvin, and A. Wallraff, Circuit quantum electrodynamics, Rev. Mod. Phys. **93**, 025005 (2021).

[14] Y. Nakamura, Y. A. Pashkin, and J. S. Tsai, Rabi oscillations in a Josephson-junction charge two-level system, Phys. Rev. Lett. **87**, 246601 (2001).

[15] J. Lisenfeld, Experiments on superconducting Josephson phase quantum bits, Ph.D. thesis, Universität Erlangen-Nürnberg, 2007.

[16] S. Ashhab, J. R. Johansson, and F. Nori, Rabi oscillations in a qubit coupled to a quantum two-level system, New J. Phys. **8**, 103 (2006).

[17] L. Garziano, R. Stassi, V. Macrì, A. F. Kockum, S. Savasta, and F. Nori, Multiphoton quantum Rabi oscillations in ultrastrong cavity QED, Phys. Rev. A **92**, 063830 (2015).

[18] A. Välimaa, W. Crump, M. Kervinen, and M. A. Sillanpää, Multiphonon transitions in a quantum electromechanical system, Phys. Rev. Appl. **17**, 064003 (2022).

[19] M. Ayyash, X. Xu, S. Ashhab, and M. Mariantoni, Driven multiphoton qubit-resonator interactions, Phys. Rev. A **110**, 053711 (2024).

[20] E. V. Stolyarov, V. L. Andriichuk, and A. M. Sokolov, Two-photon coupling via Josephson element: Breaking the symmetry with magnetic fields, Phys. Rev. B **111**, 214517 (2025).

[21] A. F. Linskens, I. Holleman, N. Dam, and J. Reuss, Two-photon Rabi oscillations, Phys. Rev. A **54**, 4854 (1996).

[22] A. M. Sokolov and F. K. Wilhelm, Superconducting detector that counts microwave photons up to two, Phys. Rev. Appl. **14**, 064063 (2020).

[23] A. M. Sokolov, Photon counting in the microwave domain and its applications to superconducting qubit readout, Ph.D. thesis, Universität des Saarlandes, 2023.

[24] W. Qin, A. F. Kockum, C. S. Muñoz, A. Miranowicz, and F. Nori, Quantum amplification and simulation of strong and ultrastrong coupling of light and matter, Phys. Rep. **1078**, 1 (2024).

[25] E. V. Stolyarov and R. A. Baskov, Detector of microwave photon pairs based on a Josephson photomultiplier, Phys. Rev. Res. **7**, 033263 (2025).

[26] S. Felicetti, J. S. Pedernales, I. L. Egusquiza, G. Romero, L. Lamata, D. Braak, and E. Solano, Spectral collapse via two-phonon interactions in trapped ions, Phys. Rev. A **92**, 033817 (2015).

[27] S. P. Fors, J. Fernández-Pendás, and A. F. Kockum, Comprehensive explanation of ZZ coupling in superconducting qubits, arXiv:2408.15402.

[28] A. Chakraborty, B. Bhandari, D. D. Briseño-Colunga, N. Stevenson, Z. Pedramrazi, C.-H. Liu, D. I. Santiago, I. Siddiqi, J. Dressel, and A. N. Jordan, Tunable superconducting quantum interference device coupler for fluxonium qubits, arXiv:2508.16907.

[29] F. Marxer, J. Mrożek, J. Andersson, L. Abdurakhimov, J. Adam, V. Bergholm, R. Beriwal, C. F. Chan, S. Dahl, S. R. Das, F. Deppe, O. Fedorets, Z. Gao, A. Gomez Frieiro, D. Gusenkova, A. Guthrie, T. Hiltunen, H. Hsu, E. Hyyppä, J. Ikonen, *et al.*, Above 99.9% fidelity single-qubit gates, two-qubit gates, and readout in a single superconducting quantum device, PRX Quantum **7**, 020333 (2026).

[30] R. Khan, F. Massel, and T. T. Heikkilä, Cross-Kerr nonlinearity in optomechanical systems, Phys. Rev. A **91**, 043822 (2015).

[31] M. Esposito, A. Ranadive, L. Planat, and N. Roch, Perspective on traveling wave microwave parametric amplifiers, Appl. Phys. Lett. **119**, 120501 (2021).

[32] Y.-F. Chen, D. Hover, S. Sendelbach, L. Maurer, S. T. Merkel, E. J. Pritchett, F. K. Wilhelm, and R. McDermott, Microwave photon counter based on Josephson junctions, Phys. Rev. Lett. **107**, 217401 (2011).

[33] L. C. G. Govia, E. J. Pritchett, S. T. Merkel, D. Pineau, and F. K. Wilhelm, Theory of Josephson photomultipliers: Optimal working conditions and back action, Phys. Rev. A **86**, 032311 (2012).

[34] A. Opremcak, I. V. Pechenezhskiy, C. Howington, B. G. Christensen, M. A. Beck, E. Leonard Jr., J. Suttle, C. Wilen,

K. N. Nesterov, G. J. Ribeill, T. Thorbeck, F. Schlenker, M. G. Vavilov, B. L. T. Plourde, and R. McDermott, Measurement of a superconducting qubit with a microwave photon counter, Science **361**, 1239 (2018).

[35] A. Opremcak, C. H. Liu, C. Wilen, K. Okubo, B. G. Christensen, D. Sank, T. C. White, A. Vainsencher, M. Giustina, A. Megrant, B. Burkett, B. L. T. Plourde, and R. McDermott, High-fidelity measurement of a superconducting qubit using an on-chip microwave photon counter, Phys. Rev. X **11**, 011027 (2021).

[36] V. I. Shnyrkov, A. P. Shapovalov, V. Y. Lyakhno, A. O. Dumik, A. A. Kalenyuk, and P. Febvre, An RF SQUID readout for a flux qubit-based microwave single photon counter, Supercond. Sci. Technol. **36**, 035005 (2023).

[37] O. A. Ilinskaya, A. I. Ryzhov, and S. N. Shevchenko, Flux qubit based detector of microwave photons, Phys. Rev. B **110**, 155414 (2024).

[38] G. Oelsner, C. K. Andersen, M. Rehák, M. Schmelz, S. Anders, M. Grajcar, U. Hübner, K. Mølmer, and E. Il'ichev, Detection of weak microwave fields with an underdamped Josephson junction, Phys. Rev. Appl. **7**, 014012 (2017).

[39] A. D'Elia, A. Rettaroli, S. Tocci, D. Babusci, C. Barone, M. Beretta, B. Buonomo, F. Chiarello, N. Chikhi, D. Di Gioacchino, G. Felici, G. Filatrella, M. Fistul, L. Foggetta, C. Gatti, E. Il'ichev, C. Ligi, M. Lisitskiy, G. Maccarrone, F. Mattioli, *et al.*, Stepping closer to pulsed single microwave photon detectors for axions search, IEEE Trans. Appl. Supercond. **33**, 1 (2023).

[40] R. Grimaudo, D. Valenti, B. Spagnolo, G. Filatrella, and C. Guarcello, Josephson-junction-based axion detection through resonant activation, Phys. Rev. D **105**, 033007 (2022).

[41] K. Inomata, Z. Lin, K. Koshino, W. D. Oliver, J.-S. Tsai, T. Yamamoto, and Y. Nakamura, Single microwave-photon detector using an artificial Λ-type three-level system, Nat. Commun. **7**, 12303 (2016).

[42] R. Lescanne, S. Deléglise, E. Albertinale, U. Réglade, T. Capelle, E. Ivanov, T. Jacqmin, Z. Leghtas, and E. Flurin, Irreversible qubit-photon coupling for the detection of itinerant microwave photons, Phys. Rev. X **10**, 021038 (2020).

[43] L. Balembois, J. Travesedo, L. Pallegoix, A. May, E. Billaud, M. Villiers, D. Estève, D. Vion, P. Bertet, and E. Flurin, Cyclically operated microwave single-photon counter with sensitivity of $10^{-22}\mathrm{W}/\sqrt{\mathrm{Hz}}$, Phys. Rev. Appl. **21**, 014043 (2024).

[44] C. Guerlin, J. Bernu, S. Deléglise, C. Sayrin, S. Gleyzes, S. Kuhr, M. Brune, J.-M. Raimond, and S. Haroche, Progressive field-state collapse and quantum non-demolition photon counting, Nature (London) **448**, 889 (2007).

[45] B. R. Johnson, M. D. Reed, A. A. Houck, D. I. Schuster, L. S. Bishop, E. Ginossar, J. M. Gambetta, L. DiCarlo, L. Frunzio, S. M. Girvin, and R. J. Schoelkopf, Quantum non-demolition detection of single microwave photons in a circuit, Nat. Phys. **6**, 663 (2010).

[46] P. J. Leek, M. Baur, J. M. Fink, R. Bianchetti, L. Steffen, S. Filipp, and A. Wallraff, Cavity quantum electrodynamics with separate photon storage and qubit readout modes, Phys. Rev. Lett. **104**, 100504 (2010).

[47] S. Kono, K. Koshino, Y. Tabuchi, A. Noguchi, and Y. Nakamura, Quantum non-demolition detection of an itinerant microwave photon, Nat. Phys. **14**, 546 (2018).

[48] A. Essig, Q. Ficheux, T. Peronnin, N. Cottet, R. Lescanne, A. Sarlette, P. Rouchon, Z. Leghtas, and B. Huard, Multiplexed photon number measurement, Phys. Rev. X **11**, 031045 (2021).

[49] R. Dassonneville, R. Assouly, T. Peronnin, P. Rouchon, and B. Huard, Number-resolved photocounter for propagating microwave mode, Phys. Rev. Appl. **14**, 044022 (2020).

[50] J. C. Curtis, C. T. Hann, S. S. Elder, C. S. Wang, L. Frunzio, L. Jiang, and R. J. Schoelkopf, Single-shot number-resolved detection of microwave photons with error mitigation, Phys. Rev. A **103**, 023705 (2021).

[51] J. Liu, H.-T. Chen, and D. Segal, Quantum nondemolition photon counting with a hybrid electromechanical probe, Phys. Rev. A **102**, 061501(R) (2020).

[52] A. Ciani, B. M. Terhal, and D. P. DiVincenzo, Hamiltonian quantum computing with superconducting qubits, Quantum Sci. Technol. **4**, 035002 (2019).

[53] G. Kim, A. Butler, and O. Painter, A tunable, modeless, and hybridization-free cross-Kerr coupler for miniaturized superconducting qubits, arXiv:2602.03186.

[54] C. Shang, H. Z. Shen, and X. X. Yi, Nonreciprocity in a strongly coupled three-mode optomechanical circulatory system, Opt. Express **27**, 25882 (2019).

[55] M. Khabipov, V. Gaydamachenko, C. Kissling, R. Dolata, and A. B. Zorin, Superconducting microwave resonators with non-centrosymmetric nonlinearity, Supercond. Sci. Technol. **35**, 065020 (2022).

[56] A. Vrajitoarea, Z. Huang, P. Groszkowski, J. Koch, and A. A. Houck, Quantum control of an oscillator using a stimulated Josephson nonlinearity, Nat. Phys. **16**, 211 (2020).

[57] J. Clarke and A. Braginski, *The SQUID Handbook* (John Wiley & Sons, Ltd, 2004).

[58] J. R. Johansson, G. Johansson, and F. Nori, Optomechanical-like coupling between superconducting resonators, Phys. Rev. A **90**, 053833 (2014).

[59] C. Eichler and J. R. Petta, Realizing a circuit analog of an optomechanical system with longitudinally coupled superconducting resonators, Phys. Rev. Lett. **120**, 227702 (2018).

[60] C. A. Potts, R. C. Dekker, S. Deve, E. W. Strijbis, and G. A. Steele, Strong intrinsic longitudinal coupling in circuit quantum electrodynamics, Phys. Rev. Lett. **134**, 153603 (2025).

[61] C. Sukumar and B. Buck, Multi-phonon generalisation of the Jaynes-Cummings model, Phys. Lett. A **83**, 211 (1981); S. Singh, Field statistics in some generalized Jaynes-Cummings models, Phys. Rev. A **25**, 3206 (1982).

[62] C. J. Villas-Boas and D. Z. Rossatto, Multiphoton Jaynes-Cummings model: Arbitrary rotations in Fock space and quantum filters, Phys. Rev. Lett. **122**, 123604 (2019).

[63] E. Jeffrey, D. Sank, J. Y. Mutus, T. C. White, J. Kelly, R. Barends, Y. Chen, Z. Chen, B. Chiaro, A. Dunsworth, A. Megrant, P. J. J. O'Malley, C. Neill, P. Roushan, A. Vainsencher, J. Wenner, A. N. Cleland, and J. M. Martinis, Fast accurate state measurement with superconducting qubits, Phys. Rev. Lett. **112**, 190504 (2014).

[64] R. Barends, J. Kelly, A. Megrant, D. Sank, E. Jeffrey, Y. Chen, Y. Yin, B. Chiaro, J. Mutus, C. Neill, P. O'Malley, P. Roushan, J. Wenner, T. C. White, A. N. Cleland, and J. M. Martinis, Coherent Josephson qubit suitable for scalable quantum integrated circuits, Phys. Rev. Lett. **111**, 080502 (2013).

[65] M. Aspelmeyer, T. J. Kippenberg, and F. Marquardt, Cavity optomechanics, Rev. Mod. Phys. **86**, 1391 (2014).

[66] T. Botter, D. W. C. Brooks, N. Brahms, S. Schreppler, and D. M. Stamper-Kurn, Linear amplifier model for optomechanical systems, Phys. Rev. A **85**, 013812 (2012).

[67] M. F. Dumas, B. Groleau-Paré, A. McDonald, M. H. Muñoz-Arias, C. Lledó, B. D'Anjou, and A. Blais, Measurement-induced transmon ionization, Phys. Rev. X **14**, 041023 (2024).

[68] T. Hillmann and F. Quijandría, Designing Kerr interactions for quantum information processing via counterrotating terms of asymmetric Josephson-junction loops, Phys. Rev. Appl. **17**, 064018 (2022).

[69] S. Bravyi, D. P. DiVincenzo, and D. Loss, Schrieffer–Wolff transformation for quantum many-body systems, Ann. Phys. (NY) **326**, 2793 (2011).

[70] C. Cohen-Tannoudji, B. Diu, and F. Laloë, *Quantum Mechanics, Volume 3: Fermions, Bosons, Photons, Correlations, and Entanglement* (Wiley-VCH, Weinheim, 2020).

[71] E. V. Stolyarov, O. V. Kliushnichenko, V. S. Kovtoniuk, and A. A. Semenov, Photon-number resolution with microwave Josephson photomultipliers, Phys. Rev. A **108**, 063710 (2023).

[72] M. F. Gely, G. A. Steele, and D. Bothner, Nature of the Lamb shift in weakly anharmonic atoms: From normal-mode splitting to quantum fluctuations, Phys. Rev. A **98**, 053808 (2018).

[73] M. H. Ansari, Superconducting qubits beyond the dispersive regime, Phys. Rev. B **100**, 024509 (2019).

[74] D. A. Bennett, L. Longobardi, V. Patel, W. Chen, D. V. Averin, and J. E. Lukens, Decoherence in rf SQUID qubits, Quantum Inf. Process. **8**, 217 (2009).

[75] N. Kosugi, S. Matsuo, K. Konno, and N. Hatakenaka, Theory of damped Rabi oscillations, Phys. Rev. B **72**, 172509 (2005).

[76] M. Steffen, M. Ansmann, R. McDermott, N. Katz, R. C. Bialczak, E. Lucero, M. Neeley, E. M. Weig, A. N. Cleland, and J. M. Martinis, State tomography of capacitively shunted phase qubits with high fidelity, Phys. Rev. Lett. **97**, 050502 (2006).

[77] R. Zhao, S. Park, T. Zhao, M. Bal, C. McRae, J. Long, and D. Pappas, Merged-element transmon, Phys. Rev. Appl. **14**, 064006 (2020).

[78] A. Osman, J. Simon, A. Bengtsson, S. Kosen, P. Krantz, D. P. Lozano, M. Scigliuzzo, P. Delsing, J. Bylander, and A. Fadavi Roudsari, Simplified Josephson-junction fabrication process for reproducibly high-performance superconducting qubits, Appl. Phys. Lett. **118**, 064002 (2021).

[79] A. Osman, J. Fernández-Pendás, C. Warren, S. Kosen, M. Scigliuzzo, A. Frisk Kockum, G. Tancredi, A. Fadavi Roudsari, and J. Bylander, Mitigation of frequency collisions in superconducting quantum processors, Phys. Rev. Res. **5**, 043001 (2023).

[80] O. W. Kennedy, K. G. Crawford, K. Shahbazi, and C. D. Shelly, Analysis of Josephson junction barrier variation: A combined electron microscopy, breakdown, and Monte Carlo approach, Phys. Rev. Mater. **9**, 084803 (2025).

[81] J. M. Kreikebaum, K. P. O'Brien, A. Morvan, and I. Siddiqi, Improving wafer-scale Josephson junction resistance variation in superconducting quantum coherent circuits, Supercond. Sci. Technol. **33**, 06LT02 (2020).

[82] L. Neumeier, M. Leib, and M. J. Hartmann, Single-photon transistor in circuit quantum electrodynamics, Phys. Rev. Lett. **111**, 063601 (2013).

[83] M. Kounalakis, C. Dickel, A. Bruno, N. K. Langford, and G. A. Steele, Tuneable hopping and nonlinear cross-Kerr interactions in a high-coherence superconducting circuit, npj Quantum Inf. **4**, 38 (2018).

[84] D. Sank, M. Khezri, S. Isakov, and J. Atalaya, Balanced coupling in electromagnetic circuits, Phys. Rev. Appl. **23**, 024012 (2025).

[85] R. Shillito, A. Petrescu, J. Cohen, J. Beall, M. Hauru, M. Ganahl, A. G. Lewis, G. Vidal, and A. Blais, Dynamics of transmon ionization, Phys. Rev. Appl. **18**, 034031 (2022).

[86] M. R. Geller, E. Donate, Y. Chen, M. T. Fang, N. Leung, C. Neill, P. Roushan, and J. M. Martinis, Tunable coupler for superconducting Xmon qubits: Perturbative nonlinear model, Phys. Rev. A **92**, 012320 (2015).

[87] J. Li, G. S. Paraoanu, K. Cicak, F. Altomare, J. I. Park, R. W. Simmonds, M. A. Sillanpää, and P. J. Hakonen, Decoherence, Autler-Townes effect, and dark states in two-tone driving of a three-level superconducting system, Phys. Rev. B **84**, 104527 (2011).

[88] M. Trif and P. Simon, Photon cross-correlations emitted by a Josephson junction in two microwave cavities, Phys. Rev. B **92**, 014503 (2015).

[89] S.-l. Ma, J.-k. Xie, Y.-l. Ren, X.-k. Li, and F.-l. Li, Photon-pair blockade in a Josephson-photonics circuit with two nondegenerate microwave resonators, New J. Phys. **24**, 053001 (2022).

[90] R. Baskov, D. K. Weiss, and S. M. Girvin, Exact amplitudes of parametric processes in driven Josephson circuits, Phys. Rev. Appl. **24**, 054038 (2025).

[91] A. Metelmann and A. A. Clerk, Nonreciprocal photon transmission and amplification via reservoir engineering, Phys. Rev. X **5**, 021025 (2015).

[92] Y.-P. Wang and C.-M. Hu, Dissipative couplings in cavity magnonics, J. Appl. Phys. **127**, 130901 (2020).

[93] V. Zakharov, S. Musher, and A. Rubenchik, Hamiltonian approach to the description of non-linear plasma phenomena, Phys. Rep. **129**, 285 (1985).

[94] A. M. Sokolov and T. T. Heikkilä, Signatures and characterization of dominating Kerr nonlinearity between two driven systems with application to a suspended magnetic beam, Phys. Rev. B **109**, 014408 (2024).

[95] M. Schöndorf, L. C. G. Govia, M. G. Vavilov, R. McDermott, and F. K. Wilhelm, Optimizing microwave photodetection: Input–output theory, Quantum Sci. Technol. **3**, 024009 (2018).

[96] R. Dassonneville, T. Ramos, V. Milchakov, L. Planat, É. Dumur, F. Foroughi, J. Puertas, S. Leger, K. Bharadwaj, J. Delaforce, C. Naud, W. Hasch-Guichard, J. J. García-Ripoll, N. Roch, and O. Buisson, Fast high-fidelity quantum nondemolition qubit readout via a nonperturbative cross-Kerr coupling, Phys. Rev. X **10**, 011045 (2020).

[97] A. A. Chapple, O. Benhayoune-Khadraoui, S. Richer, and A. Blais, Balanced cross-Kerr coupling for superconducting qubit readout, Phys. Rev. Lett. **135**, 256002 (2025).

[98] G. Beaulieu, J.-Z. Chen, M. Scigliuzzo, O. Benhayoune-Khadraoui, A. A. Chapple, P. A. Spring, A. Blais, and P. Scarlino, Fast, high-fidelity transmon readout with intrinsic Purcell protection via nonperturbative cross-Kerr coupling, PRX Quantum **7**, 033017 (2026).

[99] C. Wang, F.-M. Liu, H. Chen, Y.-F. Du, C. Ying, J.-W. Wang, Y.-H. Huo, C.-Z. Peng, X. Zhu, M.-C. Chen, C.-Y. Lu, and J.-W. Pan, Longitudinal and nonlinear coupling for high-fidelity readout of a superconducting qubit, Phys. Rev. Lett. **135**, 060803 (2025).

[100] V. B. Braginsky and F. Y. Khalili, Quantum nondemolition measurements: The route from toys to tools, Rev. Mod. Phys. **68**, 1 (1996).

[101] M. A. Sillanpää, T. Lehtinen, A. Paila, Y. Makhlin, L. Roschier, and P. J. Hakonen, Direct observation of Josephson capacitance, Phys. Rev. Lett. **95**, 206806 (2005).

[102] J. Gambetta, W. A. Braff, A. Wallraff, S. M. Girvin, and R. J. Schoelkopf, Protocols for optimal readout of qubits using a continuous quantum nondemolition measurement, Phys. Rev. A **76**, 012325 (2007).

[103] C.-F. Kam and X. Hu, Fast and high-fidelity dispersive readout of a spin qubit with squeezed microwave and resonator nonlinearity, npj Quantum Inf. **10**, 133 (2024).

[104] J. F. Chittock-Wood, R. C. C. Leon, M. A. Fogarty, T. Murphy, F.-E. von Horstig, S. M. Patomäki, G. A. Oakes, J. Williams, N. Johnson, J. Jussot, S. Kubicek, B. Govoreanu, D. F. Wise, J. J. L. Morton, and M. Fernando Gonzalez-Zalba, Radiofrequency cascade readout of coupled spin qubits, Nat. Electron. **9**, 314 (2026).

[105] C. Mori, V. Milchakov, F. D'Esposito, L. Ruela, S. Kumar, V. N. Suresh, W. Ardati, D. Nicolas, G. Cappelli, A. Ranadive, G. L. Gal, M. Esposito, Q. Ficheux, N. Roch, T. Ramos, and O. Buisson, High-power readout of a transmon qubit using a nonlinear coupling, arXiv:2507.03642.

[106] J. Gambetta, A. Blais, M. Boissonneault, A. A. Houck, D. I. Schuster, and S. M. Girvin, Quantum trajectory approach to circuit QED: Quantum jumps and the Zeno effect, Phys. Rev. A **77**, 012112 (2008).

[107] U. Patel, Y. Gao, D. Hover, G. J. Ribeill, S. Sendelbach, and R. McDermott, Coherent Josephson phase qubit with a single crystal silicon capacitor, Appl. Phys. Lett. **102**, 012602 (2013).

[108] A. P. M. Place, L. V. H. Rodgers, P. Mundada, B. M. Smitham, M. Fitzpatrick, Z. Leng, A. Premkumar, J. Bryon, A. Vrajitoarea, S. Sussman, G. Cheng, T. Madhavan, H. K. Babla, X. H. Le, Y. Gang, B. Jäck, A. Gyenis, N. Yao, R. J. Cava, N. P. de Leon, *et al.*, New material platform for superconducting transmon qubits with coherence times exceeding 0.3 milliseconds, Nat. Commun. **12**, 1779 (2021).

[109] C. Wang, X. Li, H. Xu, Z. Li, J. Wang, Z. Yang, Z. Mi, X. Liang, T. Su, C. Yang, G. Wang, W. Wang, Y. Li, M. Chen, C. Li, K. Linghu, J. Han, Y. Zhang, Y. Feng, Y. Song, *et al.*, Towards practical quantum computers: Transmon qubit with a lifetime approaching 0.5 milliseconds, npj Quantum Inf. **8**, 3 (2022).

[110] M. Tuokkola, Y. Sunada, H. Kivijärvi, J. Albanese, L. Grönberg, J.-P. Kaikkonen, V. Vesterinen, J. Govenius, and M. Möttönen, Methods to achieve near-millisecond energy relaxation and dephasing times for a superconducting transmon qubit, Nat. Commun. **16**, 5421 (2025).

[111] M. P. Bland, F. Bahrami, J. G. C. Martinez, P. H. Prestegaard, B. M. Smitham, A. Joshi, E. Hedrick, S. Kumar, A. Yang, A. C. Pakpour-Tabrizi, A. Jindal, R. D. Chang, G. Cheng, N. Yao, R. J. Cava, N. P. de Leon, and A. A. Houck, Millisecond lifetimes and coherence times in 2D transmon qubits, Nature (London) **647**, 343 (2025).

[112] L. B. Nguyen, Y.-H. Lin, A. Somoroff, R. Mencia, N. Grabon, and V. E. Manucharyan, High-coherence fluxonium qubit, Phys. Rev. X **9**, 041041 (2019).

[113] A. Somoroff, Q. Ficheux, R. A. Mencia, H. Xiong, R. Kuzmin, and V. E. Manucharyan, Millisecond coherence in a superconducting qubit, Phys. Rev. Lett. **130**, 267001 (2023).

[114] F. Wang, K. Lu, H. Zhan, L. Ma, F. Wu, H. Sun, H. Deng, Y. Bai, F. Bao, X. Chang, R. Gao, X. Gao, G. Gong, L. Hu, R. Hu, H. Ji, X. Ma, L. Mao, Z. Song, C. Tang, *et al.*, High-coherence fluxonium qubits manufactured with a wafer-scale-uniformity process, Phys. Rev. Appl. **23**, 044064 (2025).

[115] N. E. Frattini, U. Vool, S. Shankar, A. Narla, K. M. Sliwa, and M. H. Devoret, 3-wave mixing Josephson dipole element, Appl. Phys. Lett. **110**, 222603 (2017).

[116] V. L. Andriichuk, A. M. Sokolov, and E. V. Stolyarov, Computer algebra computations for "Two-photon coupling via Josephson element. II. Interaction dressing, cross-Kerr coupling, and limits of low-energy bosonic model", Zenodo, 2026, doi:10.5281/zenodo.23229231.

[117] G. Zhu, D. G. Ferguson, V. E. Manucharyan, and J. Koch, Circuit QED with fluxonium qubits: Theory of the dispersive regime, Phys. Rev. B **87**, 024510 (2013).

[118] D. Lamberto, A. Mercurio, O. Di Stefano, V. Savona, and S. Savasta, Renormalization and low-energy effective models in cavity and circuit quantum electrodynamics, Commun. Phys. **8**, 430 (2025).

[119] J. Feist *et al.*, QuantumAlgebra.jl (2021), https://github.com/jfeist/QuantumAlgebra.jl.

[120] L. D. Landau and E. M. Lifshits, *Quantum Mechanics: Non-Relativistic Theory*, 3rd ed. (Pergamon Press, Oxford, 1991).

[121] J. Mauricio Torres, C. Ventura-Velázquez, and I. Arellano-Melendez, Perfect revivals of Rabi oscillations and hybrid Bell states in a trapped ion, J. Phys. B: At., Mol. Opt. Phys. **58**, 065502 (2025).

[122] G. C. Wick, The evaluation of the collision matrix, Phys. Rev. **80**, 268 (1950).

[123] P. Blasiak, A. Horzela, K. A. Penson, A. I. Solomon, and G. H. E. Duchamp, Combinatorics and Boson normal ordering: A gentle introduction, Am. J. Phys. **75**, 639 (2007).

[124] H. M. Lim, D. Dwiputra, M. S. Ukhtary, and A. R. T. Nugraha, pyBoLaNO: A Python symbolic package for normal ordering involving bosonic ladder operators, Comput. Phys. Commun. **313**, 109622 (2025).

[125] P. Blasiak, Combinatorics of boson normal ordering and some applications, Ph.D. thesis, Institute of Nuclear Physics of Polish Academy of Sciences and Université Pierre et Marie Curie, arXiv:quant-ph/0507206.

[126] M. A. Méndez, P. Blasiak, and K. A. Penson, Combinatorial approach to generalized Bell and Stirling numbers and boson normal ordering problem, J. Math. Phys. **46**, 083511 (2005).

[127] D. Zueco, G. M. Reuther, S. Kohler, and P. Hänggi, Qubit-oscillator dynamics in the dispersive regime: Analytical theory beyond the rotating-wave approximation, Phys. Rev. A **80**, 033846 (2009).

[128] K. Petrovnin, J. Wang, M. Perelshtein, P. Hakonen, and G. S. Paraoanu, Microwave photon detection at parametric criticality, PRX Quantum **5**, 020342 (2024).